ISSN 2095-9281 (网络)
ISSN 2095-9273 (印刷)
科学通报 (英文版)

Science Bulletin

Volume 68 · Number 19 · October 2023

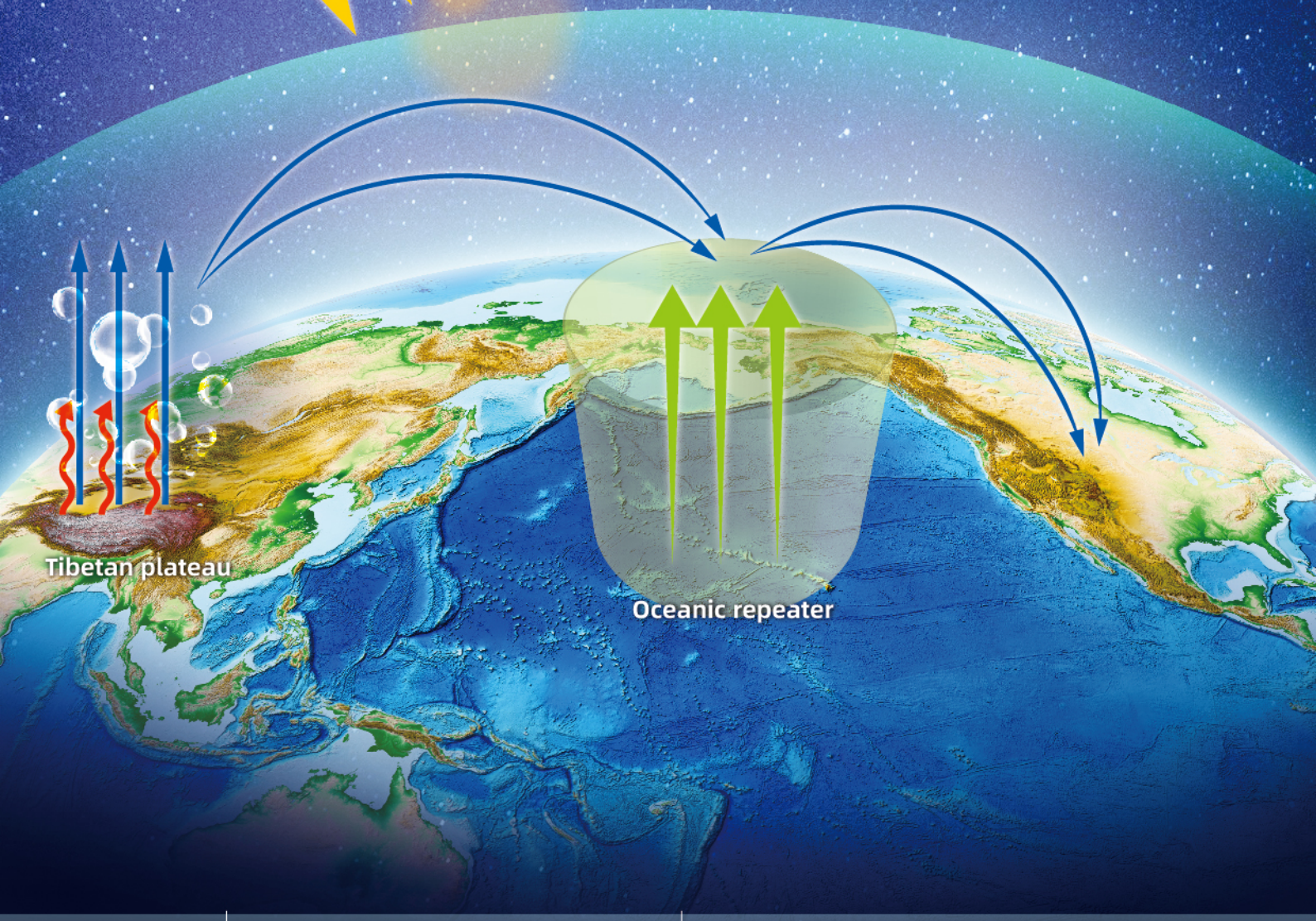

ELSEVIER
SCIENCE CHINA PRESS
Chinese Academy of Sciences
National Natural Science Foundation of China

Science Bulletin 68 (2023) 2225–2235

Contents lists available at ScienceDirect

Science Bulletin

journal homepage: www.elsevier.com/locate/scib

Article

Oceanic repeaters boost the global climatic impact of the Tibetan Plateau

Yongkun Xie [a], Jianping Huang [a,*], Guoxiong Wu [b,c,*], Yimin Liu [b,c], Wenhao Dong [d,e], Mengmeng Lu [f,g], Bian He [b,c], Zifan Su [a,h], Qing Bao [b,c], Qingyun Zhao [a], Yuzhi Liu [a]

[a] Collaborative Innovation Center for Western Ecological Safety, Lanzhou University, Lanzhou 730000, China
[b] State Key Laboratory of Numerical Modeling for Atmospheric Sciences and Geophysical Fluid Dynamics (LASG), Institute of Atmospheric Physics, Chinese Academy of Sciences, Beijing 100029, China
[c] College of Earth and Planetary Sciences, University of Chinese Academy of Sciences, Beijing 100049, China
[d] NOAA/Geophysical Fluid Dynamics Laboratory, Princeton NJ 08542, USA
[e] Cooperative Programs for the Advancement of Earth System Science, University Corporation for Atmospheric Research, Boulder CO 80301, USA
[f] State Key Laboratory of Severe Weather and Institute of Tibetan Plateau Meteorology, Chinese Academy of Meteorological Sciences, Beijing 100081, China
[g] Southern Marine Science and Engineering Guangdong Laboratory (Zhuhai), Zhuhai 519000, China
[h] College of Atmospheric Sciences, Lanzhou University, Lanzhou 730000, China

ARTICLE INFO

Article history:
Received 24 December 2022
Received in revised form 30 June 2023
Accepted 30 June 2023
Available online 14 July 2023

Keywords:
Tibetan Plateau
Oceanic repeater
Global climate
Air-sea interactions
Pacific and Atlantic Oceans

ABSTRACT

The topography of the Tibetan Plateau (TP) has shaped the paleoclimatic evolution of the Asian monsoon. However, the influence of the TP on the global climate, beyond the domain of the Asian monsoon, remains unclear. Here we show that the Pacific and Atlantic Oceans act as efficient repeaters that boost the global climatic impact of the TP. The simulations demonstrate that oceanic repeaters enable TP heating to induce a wide-ranging climate response across the globe. A 1 °C TP warming can result in a 0.73 °C temperature increase over North America. Oceanic repeaters exert their influence by enhancing the air-sea interaction-mediated horizontal heat and moisture transport, as well as relevant atmospheric circulation pathways including westerlies, stationary waves, and zonal-vertical cells. Air-sea interactions were further tied to local feedbacks, mainly the decreased air-sea latent heat flux from the weakening air-sea humidity difference and the increased shortwave radiation from sinking motion-induced cloud reduction over the North Pacific and Atlantic Oceans. Our findings highlight the crucial influence of TP heating variation on the current climate under a quasi-fixed topography, in contrast to topography change previously studied in paleoclimate evolution. Therefore, TP heating should be considered in research on global climate change.

1. Introduction

The impact of the Tibetan Plateau (TP) topography on climate has been investigated for more than one and one-third centuries [1]. Early research has focused on atmospheric circulations [1–3], especially the influence of the TP on the surrounding Asian monsoon and desert regions [4–6]. By influencing atmospheric circulations, the uplift of the TP topography has been suggested to have shaped the stages in the paleoclimate evolution of the Asian monsoon and formation of the Central Asian desert [4–9]. Atmospheric circulation models without ocean coupling were used in early research. Therefore, the influence of the TP uplift on remote regions beyond Asia and the pertinent effects of oceans have not been extensively studied in the early research.

The influence of the TP uplift on oceans was first investigated three decades ago [10]. However, only the ocean surface, namely the sea surface temperature or mixed layer, was examined [10,11]. The ocean models used were simple slab ocean models with a 50 m mixed layer. Two decades ago, fully coupled oceanic circulation models were used to examine the influence of the TP uplift on the ocean [12]. Subsequently, the feedback of the coupled ocean on the climate effect of TP uplift was investigated [13]. However, these simulations were integrated for $\leq$50 years [12,13], which are not sufficient for large-scale oceanic circulation to reach an equilibrium state, especially in response to strong paleoclimatic forcing, such as topography modification [14–16].

Therefore, the influence of the TP uplift on the ocean or the reverse feedback of the ocean should be further investigated using updated simulations. Recently, the influence of the TP uplift on oceans was investigated using fully coupled climate models that have been integrated for long periods of 4 to 18 centuries

* Corresponding authors.
E-mail addresses: hjp@lzu.edu.cn (J. Huang), gxwu@lasg.iap.ac.cn (G. Wu).

https://doi.org/10.1016/j.scib.2023.07.019
2095-9273/

[14–16]. These long-term integrated simulations have suggested that the TP uplift was crucial for the formation of the modern Atlantic Meridional Overturning Circulation and collapse of the Pacific Meridional Overturning Circulation, which was also suggested by paleoclimate records [17]. Therefore, regarding the overall effect of the TP topography, the role of large-scale oceanic circulation is crucial and needs to be considered. However, the paleoclimatic impact of the TP uplift on large-scale oceanic overturning circulation has limited implications for current climate variability. This is because topography can be considered quasi-fixed in the context of the modern climate. In contrast, the effect of TP heating or thermal forcing is of considerable importance, because TP heating has shown pronounced variability across scales from interseasonal to interdecadal [18,19]. In addition to pure mechanical forcing [20–24], TP heating has been suggested to be crucial for the Asian summer monsoon [25–28].

Studies on the effect of air-sea interactions on the climate effect of the TP have increased in the last five years [29–32]. These studies have focused on the Asian monsoon regions [30], tropics of the Asia–Pacific [29], North Pacific Ocean [31], and Atlantic Ocean [32]. Regarding studies on regions beyond Asia, some have focused on the paleoclimatic TP uplift [29]. Therefore, the role of TP heating was not separated from that of the mechanical forcing. The study of the North Pacific Ocean has been limited to the spring and Asia–Pacific regions [31]. The study on the Atlantic Ocean examined the isolated role of Atlantic sea surface temperatures in modulating the effect of TP heating on the climate [32], wherein TP heating was modified by modifying the surface albedo. Given that the response of the atmospheric circulation to heating anomalies in different Tibetan Plateau domains may vary [33], the discrepancies between the locations of heating anomalies in albedo-modification-based simulations [32–34] and in observations (Section 2.2) have indicated that studies using albedo-modification-based simulations have limited implications for the current climate variability.

Therefore, the influence of TP heating on the global climate beyond Asian monsoon regions and pertinent air-sea interactions, focusing on the current climate rather than the paleoclimate, has not been previously studied. This study aims to advance the Asian monsoon-centered knowledge of the climate effect of TP heating to a global scale and determine the role of air-sea interactions using updated numerical simulations that are constrained by current observations. To improve robustness, simulations from the global monsoons model inter-comparison project (GMMIP) [35] were used.

2. Data and methods

2.1. Data

GPCP observational precipitation data were obtained from the NOAA/OAR/ESRL PSL [36]. The observational near-surface air temperature data were GISTEMP from NASA/GISS [37]. The reanalysis data were ERA5 [38], provided by ECMWF, and NCEP-2 [39], provided by NCEP/DOE. All the data were monthly mean. Additional details regarding the data, numerical simulations, and statistical methods are provided in the Supplementary materials (online).

2.2. Numerical simulations

Two groups of numerical simulations were examined, that is, GMMIP [35,40–42] experiments from the coupled model inter-comparison project in the 6th phase (CMIP6) and the community Earth system model (CESM) experiments we performed (Table S1 online). There were two GMMIP experiments, namely amip-hist and amip-TIP-nosh, where TIP indicates Tibetan–Iranian Plateau coupling system. There were six CESM experiments, namely amip-hist, amip-TIP-nosh, amip-TIP-alb0.5, amip-TIP-sh0.5, cmip-hist, and cmip-TIP-sh0.5. The CESM model (version 2.1.3) was provided by NCAR/UCAR [43]. In all the experiments, historical (hist) experiments were control runs, whereas the TIP-labeled experiments were sensitivity runs. As shown in Fig. S1 (online), the control runs could reproduce the current climate in the observations from 1979 to 2014, thereby assuring the basis for further analyses of the sensitivity runs.

The benchmark amip-TIP-nosh (no sensible heat) experiment removed the sensible heat over the Asian topographies above 500 m as shown in Fig. 1a, i.e., TIP [35]. Modifying topography or heating over the large domain could avoid artificial forcing from the sharp topography or heating gradients when a cut-off was suddenly implemented [35]. Consequently, the magnitude of the temperature changes was the largest over the TIP and gradually decreased outward (Fig. 1a). Given that the largest changes were over the high elevation plateau such as 1.5 km (Fig. 1a), the atmospheric circulation response could still be predominantly attributed to the TIP when higher criteria than 500 m were used to identify the plateau.

For technical details, the sensible heat, that is, vertical diffusive heat [22], on the entire column of the atmosphere was modified in each time step of model integration. This assured the vertical continuity of total diabatic heating of the atmosphere. Therefore, the term "sensible heat" in the experimental designs was not the same as the single level "sensible heat flux" at the surface. Given that the feedbacks were fully active, the response to the sensible heat modification in the experiments was not solely from sensible heat but also the pertinent feedbacks that influenced the total diabatic heating of the atmosphere, that is, TP heating, such as the land–atmosphere coupling processes, vertical motion-induced adiabatic heating, and longwave cooling [44,45]. Our method was different from that of FGOALS-f3-L, which set the vertical temperature diffusion term to zero in the atmospheric thermodynamic equation at the bottom boundary layer [41]. However, the results were consistent, as shown in Section 3.1.

The amip-TIP-alb0.5 (half albedo) experiment used a distinct method from that used in sensible heat-based experiments to modify TP heating. The spatial pattern of anomalous TP heating reflected by temperature in the albedo-based experiment was mainly determined by the snow cover where the albedo was high (Fig. S2 online). Therefore, in the albedo-based experiment, the variation in TP heating was substantial only during the cold season, whereas the observed variation in TP heating was strong in all the seasons (Fig. S3 online). The variability observed in TP heating was large around the southern slope because of the sensible heat (Fig. S3 online). Meanwhile, a substantial variation was observed over the central platform in the albedo-based experiment (Fig. S2 online). In contrast, the sensible heat-based experiments showed greater similarity with observations in spatial patterns and seasonality, because sensible heat was an important part of the total heating (Fig. S3 online).

Therefore, the sensible heat-based experiments were better at representing the characteristics observed in TP heating than the albedo-based experiments. The heating forcing was far stronger in the non-sensible heat experiment than in the variability range observed. Based on the observational constraint concept, a half-sensible heat experiment (sh0.5) was designed to simulate the current climate more effectively. TP heating anomalies in the half-sensible heat experiment correspond to a 2.5 °C average warming over the TP, which is within the range observed for current TP climate variations, thereby having direct implications for the current climate. Nonetheless, for the highest level of robustness, the nosh experiment based on multiple models was examined in Section 3.1

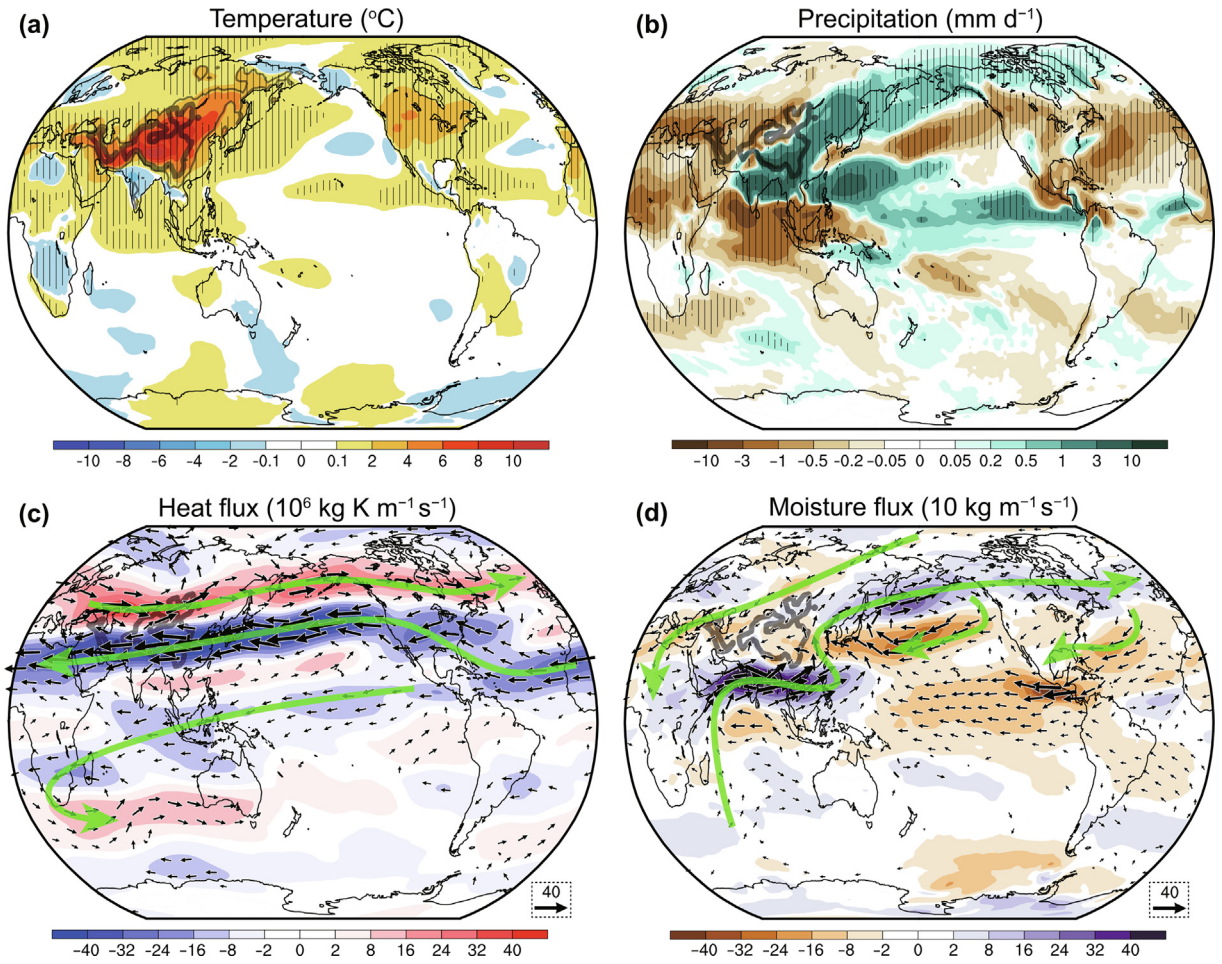

Fig. 1. Impact of TP heating on temperature, precipitation, and horizontal heat and moisture transport in summer. Differences in June to August (JJA) mean near-surface air temperature (a) and precipitation (b) determined using amip-hist minus amip-TIP-nosh for 1979–2014. The stripe in (a) and (b) indicates both the significant differences at the 95% confidence level and the consistent signs across three models. Differences in JJA mean vertically-integrated horizontal heat (c) and moisture flux (vector) (d) and their zonal components (color shading) determined using amip-hist minus amip-TIP-nosh from CESM for 2000–2014 (Section 2.3). The vectors with insignificant (95% confidence level) differences in both zonal and meridional components were not shown in (c) and (d); the green arrows indicate the pathways of heat or moisture flux. The thick grey contour indicates 1.5 km elevation, while the thin grey contour in (a) indicates 500 m elevation.

because the GMMIP has the nosh experiment but no sh0.5 experiment. The amip-labeled experiments used atmospheric circulation models without ocean coupling, whereas the cmip-labeled experiments used fully coupled climate models. The differences between the cmip and amip experiments indicate the role of the air-sea interactions. The concepts underlying the experimental designs addressed above are schematically summarized in Fig. S4 (online). The amip and cmip simulations were analyzed for 1979–2014 and 1850–2014 based on monthly outputs, respectively, except for the horizontal heat and moisture flux of the atmosphere which was analyzed for 2000–2014 based on three-hourly outputs.

2.3. Horizontal heat and moisture flux of the atmosphere

The horizontal heat flux was formulated as $\vec{H} = \rho\vec{V}\theta$, where ρ, $\vec{V}$, and θ indicate the density, horizontal velocity, and potential temperature of the atmosphere, respectively. The vertically integrated horizontal heat flux was calculated according to the formula $\{\vec{H}\} = \int_0^\infty \vec{H}\mathrm{d}z = -\frac{1}{g}\int_{p_s}^0 \vec{V}\theta\mathrm{d}p$, where g, p, and p_s indicate the acceleration of gravity, pressure, and surface pressure, respectively. The horizontal moisture flux was formulated as $\vec{M} = \rho\vec{V}q$, where q indicates the specific humidity. The vertically integrated horizontal moisture flux was $\{\vec{M}\} = \int_0^\infty \vec{M}\mathrm{d}z = -\frac{1}{g}\int_{p_s}^0 \vec{V}q\mathrm{d}p$. Given that the flux is nonlinear, we calculated the heat and moisture flux using the three-hourly output from 2000 to 2014. The high-frequency outputs were only available for 15 years because of the large storage cost.

2.4. Energy budget of the ocean mixed layer and sea surface

The energy budget of the ocean mixed layer is based on the potential temperature (θ) tendency equation of the mixed layer, which is represented as a 0–50 m subsurface ocean as follows:

$$\underbrace{[\partial_t\theta]}_{\mathrm{TEND}} = \underbrace{-[\vec{V}\cdot\nabla_h\theta]}_{\mathrm{ADV}} \underbrace{-[w\partial_z\theta]}_{\mathrm{MIX}} + \underbrace{\frac{E^{\downarrow}_{\mathrm{net}} - E^{\downarrow}_{\mathrm{pen}}}{\rho_0 c_p H}}_{\mathrm{ENE}} + \varepsilon, \quad (1)$$

where $\vec{V}$ and w indicate the horizontal and vertical velocities, respectively. $E^{\downarrow}_{\mathrm{net}}$ indicates the net atmospheric energy input at the sea surface, as indicated by Eq. (2).

The energy budget at the sea surface is formulated as follows:

$$E^{\downarrow}_{\mathrm{net}} = \underbrace{SW^{\downarrow} - SW^{\uparrow}}_{SW^{\downarrow}_{\mathrm{net}}} + \underbrace{LW^{\downarrow} - LW^{\uparrow}}_{LW^{\downarrow}_{\mathrm{net}}} + SH^{\downarrow} + LH^{\downarrow}, \quad (2)$$

where *SW*, *LW*, *SH*, and *LH* indicate shortwave/longwave radiation and sensible/latent heat flux, respectively, and the arrows indicate the downward and upward directions, respectively. $E^{\downarrow}_{\text{pen}}$ indicates the energy penetrating the mixed layer inferred from the downward shortwave radiation at the sea surface, as Eq. (7) in Ref. [30]; ρ_0, c_p, and H indicate the density, specific heat, and depth of the mixed layer, respectively [30]. The $E^{\downarrow}_{\text{pen}}$ can be inferred from the downward shortwave radiation because shortwave radiation was less reflected at the sea surface. The empirical formulation was based on observations over the Pacific [46]. The left-hand term is the local tendency term of the potential temperature (TEND) calculated as the potential temperature difference between two sequential months and in units of K month^{-1} [30,31]. Meanwhile, the right-hand terms are the potential temperature tendency induced by horizontal advection (ADV), vertical mixing (MIX), atmospheric energy input (ENE), and the residual term (ε). The symbol $[\,] = \frac{1}{H}\int_0^H \mathrm{d}z$ indicates the vertical mean across the mixed layer.

Based on the bulk parameterizations [47], the latent heat flux at the sea surface is proportional to the air-sea humidity difference and near-surface wind speed. The air-sea humidity difference is defined as the saturation specific humidity at the sea surface minus the specific humidity of near-surface air, namely, $q_s(T_s)$–q_a; $q_s(T_s)$ is saturation specific humidity at sea surface temperature (T_s) calculated as $q_s = 0.622e_s/(p–e_s)$ [48], where e_s was calculated as Eq. (17) of Ref. [49] and p indicates pressure.

2.5. Statistical methods

The statistical significance of the differences between the control and sensitivity runs was estimated using two-tailed Student's *t*-test. For the multiple model results, the overall significance of the results was jointly estimated using a *t*-test of the ensemble mean differences and the consistency of the signs in differences across the models. The Pearson sample linear cross-correlation coefficient was used to examine the correlation between two variables. The statistical significance of the linear correlation coefficient was determined using a two-tailed Pearson's *r*-test.

3. Results

3.1. Atmospheric response without ocean coupling

Given that the TP heating was strongest in the summer (Fig. S3 online), only the summer situation was examined. Multimodel simulations (amip-hist minus amip-TIP-nosh) from GMMIP and CESM demonstrated a robust response of the atmosphere to TP heating without ocean coupling. Relative to previous studies that used single model-based simulations, the robustness of the results was enhanced by consistency among the three models. TP heating induced significant changes in temperature over many regions of the Northern Hemisphere (Fig. 1a), which were positive over most regions. In the observations, the TP temperature was also positively correlated with the temperature over many regions across the globe (Fig. S5 online). The following analysis made advancements with respect to previous studies by separating the individual effect of TP heating from the overall effect of TP or extending the Asian monsoon-centered research to the global scale. Outside the TP and its surroundings, the most prominent positive temperature changes occurred over North America. The temperature changes averaged over the TP and North America were approximately 8 and 3 °C, respectively, with a response-to-forcing ratio of 3/8. The positive correlation between temperature over the TP and North America was also significant concerning year-to-year variability in observations (Fig. S5 online). For the other regions, although they were robust with consistent signs among models and statistically significant, the response-to-forcing ratio was relatively low.

In line with the findings of previous studies [25,27,33], TP heating significantly increased precipitation over most of the Asian monsoon regions (Fig. 1b). However, the results indicated that the change in precipitation around the south of the TP and over the belt from the lower Yangtze River to Japan was statistically insignificant. Outside the TP, TP heating significantly suppressed precipitation over the regions from Central Asia to Europe and Africa and from the mid-latitudes of the North Pacific to the Atlantic and North Indian Ocean. TP heating increased precipitation over the western subtropical Pacific, eastern tropical Pacific, and high latitudes from the North Pacific to North America.

Why the TP heating could have a near-global influence on temperature and precipitation was explained by the horizontal heat and moisture transport and the three-dimensional circulation of the atmosphere (Figs. 1c, d and 2). The TP heating disturbed the global heat and moisture transport along the three and four green arrow-marked pathways in Fig. 1c, d, respectively. The subtropical westward and extratropical eastward belts of the heat flux (Fig. 1c) jointly determined the influence of TP heating on large-scale circulation (Fig. 2) across the Northern Hemisphere, especially, the upper-level anticyclonic circulation occupying the Northern Hemisphere (Fig. 2c). The other weaker branch from the tropics to the Southern Hemisphere determined the weaker influence of the TP heating on the Southern Hemisphere. Regarding precipitation, the northward belt of the moisture flux (Fig. 1d) determined the increased precipitation from South Asia to North America and the western subtropical Pacific (Fig. 1b). In contrast, the three southward belts determined the decreased precipitation over Central Asia, Europe, Africa, and North Pacific and Atlantic Oceans.

Besides the thermodynamic factor of moisture supply (Fig. 1d), precipitation anomalies were also dynamically constrained by changes in the vertical motion (Figs. 1b and 2a); that is, the ascending/sinking motion corresponds to more/less precipitation. For regions of Central Asia, Europe, Africa, and the North Pacific and Atlantic Oceans, the sinking motion and reduced moisture from southward dry air flow jointly influenced the decreased precipitation. In contrast, the enhanced moisture supply of the Asian summer monsoon [25] partially offset the influence of the sinking motion from East China to Japan on precipitation. Therefore, a precipitation decrease was observed in a smaller area relative to the area of sinking motion (Figs. 1b, d and 2a).

Over the Asian monsoon regions, the TP heating-driven ascending motion rendered the large-scale circulation baroclinic, namely the opposite in the lower and upper levels (Fig. 2b, c). This baroclinic structure is explained by the TP heating-driven air-pump mechanism [22,25,27,45] as follows: TP heating triggered near-surface convergence, cyclonic circulation (Fig. 2b), and ascending motion (Fig. 2a). The feedback of condensation latent heat from precipitation (Fig. 1b) further promoted the vertical motion and upper-level anticyclone (Fig. 2c). The increased precipitation in the western subtropical Pacific (Fig. 1b) was also associated with a baroclinic structure (Fig. 2b, c) and was further facilitated by more moisture supply (Fig. 1d). The TP heating-induced strong vertical motion generated zonal- or meridional-vertical circulation cells [34,45,50–54] ascending from the TP. The sinking branch of the zonal- and meridional-vertical cells was over the regions of Central Asia/Europe/Africa and the North Indian Ocean, respectively (Fig. 2a). The North Indian Ocean sinking branch may also have contributed to the increased precipitation in the eastern tropical Pacific via tropical Walker circulation [55] (Figs. 1b and 2a).

Outside the Asian monsoon regions, large-scale circulation was generally barotropic (Fig. 2b, c). This was constrained by the circulation development associated with disturbances in the westerlies, jet streams, and stationary waves [56,57]. Corresponding to the

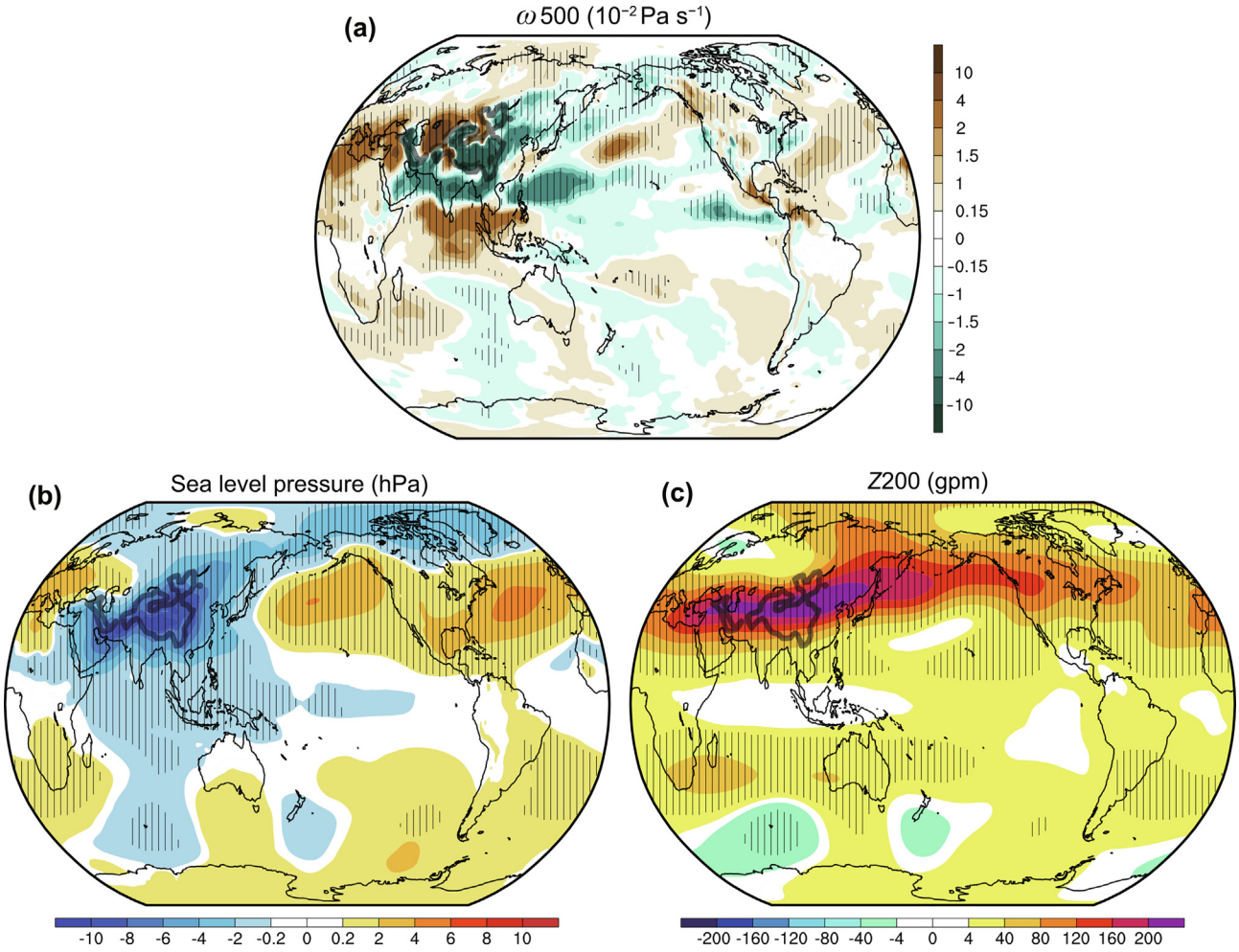

Fig. 2. Impact of TP heating on atmospheric circulations in summer. Differences in JJA mean vertical velocity in isobaric coordinate at 500 hPa (ω500) (a), sea level pressure (b), and geopotential height at 200 hPa (Z200) (c) determined using amip-hist minus amip-TIP-nosh for 1979–2014. The positive and negative values in (a) indicate sinking and ascending motions, respectively. The stripe indicates both the significant differences at the 95% confidence level and the consistent signs across three models. The thick grey contour indicates 1.5 km elevation.

two belts of the heat flux (Fig. 1c), the TP heating induced the upper-level anticyclonic circulation to develop into a prominent high-pressure belt occupying the Northern Hemisphere (Fig. 2c). This upper-level circulation was coupled with low-level circulation in a barotropic structure, such as high sea level pressure from the Pacific to the Atlantic (Fig. 2b). For those barotropic structures, the low-pressure system generally corresponded to the ascending motion, whereas the high-pressure system corresponded to the sinking motion (Fig. 2).

Therefore, the high pressure in the North Pacific and Atlantic Oceans corresponded to sinking motion (Fig. 2) and decreased precipitation (Fig. 1b). Meanwhile, the low pressure at the high latitudes of the North Pacific and North America corresponded to ascending motion and increased precipitation, in which the upper-level pressure was low relative to the same latitude. The change in the extratropical Southern Hemisphere was a classic barotropic stationary wave pattern (Fig. 2) and corresponded to the heat flux belt from the tropics to Southern Hemisphere (Fig. 1c). This wave was also observed in the experiments removing the TP topography [58], which further suggested that the anomalies over the Indian Ocean were crucial for the TP-induced wave train in Southern Hemisphere.

Regarding temperature over land, the significant warm temperature in North America, Europe, and Africa (Fig. 1a) was associated with high pressure and sinking motion (Fig. 2). The warm temperature over the North Indian Ocean was also induced by the sinking motion. Meanwhile, the warm temperature over the western Pacific was associated with the downstream advection of TP heating (Fig. 1c) and sinking motion (Fig. 2a) in the north and south flanks, respectively. However, given that the air temperature over the ocean was constrained by the prescribed sea surface temperature, the influence of TP heating on the temperature over the ocean was investigated further using coupled experiments, the results of which are presented in the next section.

3.2. Effect of air-sea interactions

To shed light on the current climate, the effect of air-sea interactions was investigated using half-sensible heat experiments. The primary differences between the amip and cmip experiments were not in the patterns but in the magnitudes (Fig. 3a, b). The all-positive and all-negative configurations in the signs of cmip, amip, and cmip minus amip indicate the amplification effect of air-sea interactions on the magnitudes. Air-sea interactions amplify anomalous temperature magnitudes over the TP and remote regions, especially in the downstream Pacific, North America, and Atlantic regions (Fig. 3a). However, the ratios of magnitude amplification were substantially stronger

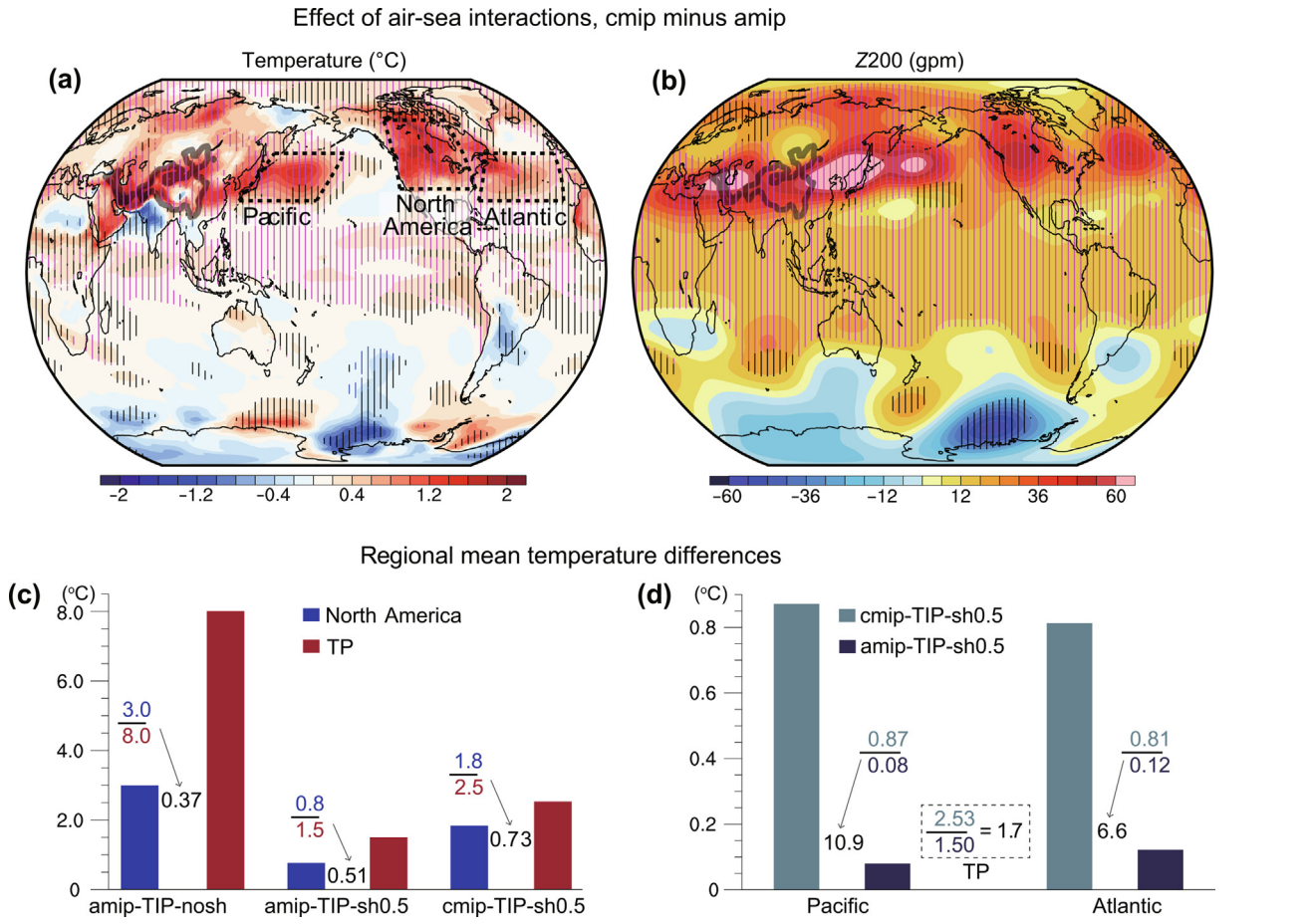

Fig. 3. Effect of air-sea interactions. Differences in JJA mean near-surface air temperature (a) and *Z*200 (b) determined using cmip (cmip-hist minus cmip-TIP-sh0.5) minus amip (amip-hist minus amip-TIP-sh0.5) experiments for 1850–2014 (Fig. S6 online). The stripe indicates significant differences in cmip minus amip at the 95% confidence level; the red and blue colors further indicate all-positive and all-negative configurations in the signs of cmip, amip, and cmip minus amip, suggesting consistency in patterns. The thick grey contour indicates 1.5 km elevation. The dashed polygons indicate domains examined in (c) and (d). (c) Regional mean temperature differences averaged over North America and TP above 1.5 km, using amip-hist minus amip-TIP-nosh or amip-TIP-sh0.5, and cmip-hist minus cmip-TIP-sh0.5 experiments, respectively. The ratios of temperature differences between the two regions are marked. (d) Regional mean temperature differences averaged over the Pacific and Atlantic Oceans by using cmip-hist minus cmip-TIP-sh0.5 and amip-hist minus amip-TIP-sh0.5, respectively. Shown in the box was the regional mean temperature averaged over the TP above 1.5 km.

over the remote regions than over the TP (Fig. 3c, d). The amplification effect of air-sea interactions increases the response-to-forcing ratio of remote regions with respect to TP. The ratio of anomalous temperature in North America relative to that in the TP was 0.37 or 0.51 without air-sea interactions, and this ratio increased to 0.73 when active air-sea interactions were involved (Fig. 3c).

The most prominent differences were over the downstream oceans (Fig. 3a), indicating that air-sea interactions over the Pacific and Atlantic Oceans are crucial for modulating the climate impact of TP heating. Air-sea interactions amplified the temperature changes over the Pacific and Atlantic by 10.9 and 6.6 times, respectively, in contrast to 1.7 times over the TP (Fig. 3d). Furthermore, air-sea interactions amplified the TP heating-induced high-pressure anomalies in the westerlies of the Northern Hemisphere (Fig. 3b) and the corresponding pathways of horizontal heat transport (Fig. 1c and Fig. S7a online). Outside the TP regions, the most prominent amplifications in upper-level circulation were also centered over the western North Pacific, North America, and Atlantic. Here, the magnitudes gradually decayed from the Pacific to the Atlantic (Fig. 3b). Therefore, we concluded that the Pacific and Atlantic Oceans act as two repeaters that amplify TP heating-induced disturbances from near to distant locations via air-sea interactions.

Air-sea interactions also amplified the magnitudes of the large-scale patterns of sea level pressure and vertical motion (Fig. S8 online), except for the Indian Ocean. The sinking motion of the zonal-vertical cell from the TP to upstream Central Asia, Europe, and Africa and the barotropic high pressure over the North Pacific and Atlantic Oceans became stronger (Fig. 3b and Fig. S8 online). However, the air-sea interactions over the Indian Ocean generated an indirect meridional-vertical cell that is opposite to the meridional-vertical cell directly induced by TP heating [30]. Therefore, in contrast to the Pacific and Atlantic Oceans, the Indian Ocean is not an effective repeater, because it partially offsets the direct effect of TP heating.

The physical processes of the air-sea interactions over the Pacific and Atlantic Oceans were examined further. In line with the near-surface air temperature anomalies (Fig. 3a), upper-layer subsurface ocean temperature anomalies were the most evident in the North Pacific and Atlantic Oceans (Fig. S9 online). Based on the energy budget of the ocean mixed layer (0–50 m) and sea surface (Fig. 4), the factors contributing to ocean temperature changes were determined. The amplified warming in the Pacific and Atlantic Oceans was dominated by enhanced atmospheric energy input (Fig. 4a; Eq. (1)), which indicated that air-sea interaction processes determined the mixed layer temperature changes rather than the internal oceanic advection and mixing processes.

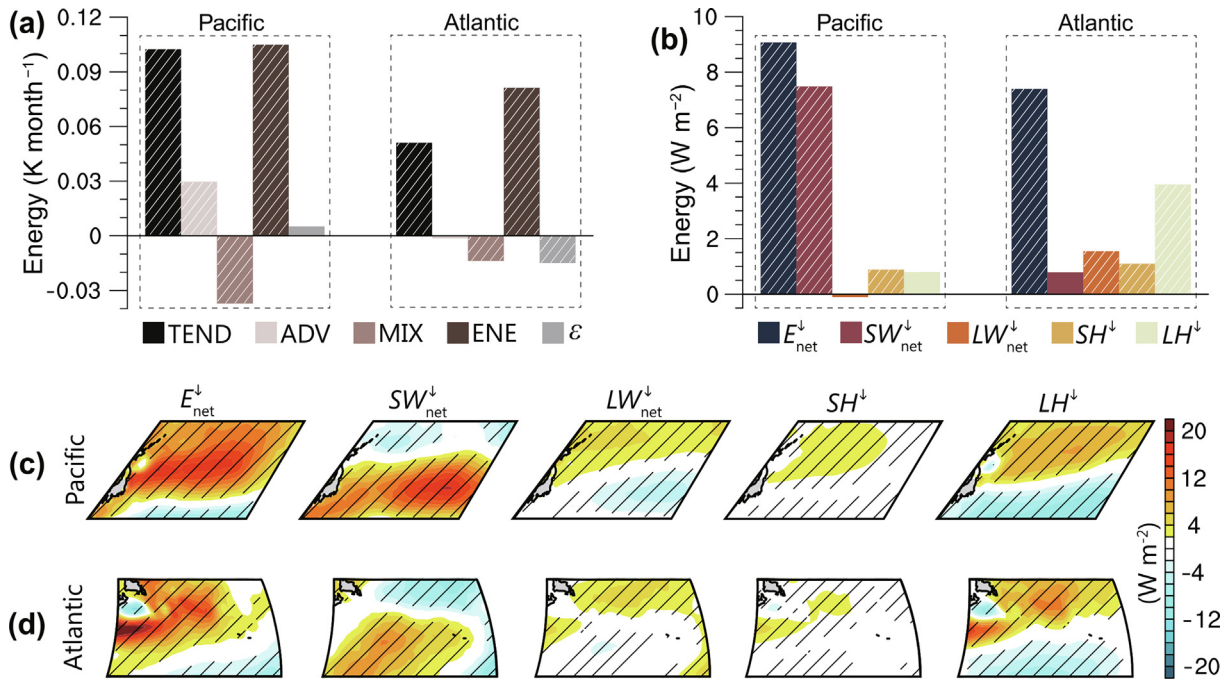

Fig. 4. Physical processes underlying the air-sea interactions of the oceanic repeaters. (a) Differences in JJA mean energy budget terms (Eq. (1)) of mixed layer averaged over the Pacific and Atlantic domains shown in Fig. 3a, determined using cmip-hist minus cmip-TIP-sh0.5 experiments for 1850–2014. (b) Same as (a) but for energy budget terms (Eq. (2)) of sea surface averaged over the Pacific and Atlantic domains with positive values in $E^{\downarrow}_{net}$ of (c) and (d), respectively. (c), (d) Spatial patterns of energy budget terms at the sea surface corresponding to (b) for the Pacific and Atlantic Oceans, respectively. The stripe indicates significant differences at the 95% confidence level.

The atmospheric energy input term is equal to and larger than the potential temperature tendency term for the Pacific and Atlantic Oceans, respectively (Fig. 4a). Vertical potential temperature mixing weakened the warming of the mixed layer by transporting the input energy to the deeper ocean. The horizontal potential temperature advection and residual terms contribute positively and negatively, respectively, to the Pacific and Atlantic Oceans. However, the horizontal advection and residual terms had small-scale signals that were inconsistent with the potential temperature tendency term (Fig. S10 online). In contrast, the spatial pattern of atmospheric energy input resembles that of the potential temperature tendency. Moreover, the balance relation among the energy budget terms was not sensitive to other subset periods chosen to examine, as indicated by the time-series shown in Fig. S11 (online). Therefore, the dominance of atmospheric energy input was demonstrated by the regional mean magnitudes and spatial patterns (Fig. 4a and Fig. S10 online).

Although the regional mean results were different (Fig. 4b), the dominant processes contributing to anomalous atmospheric energy inputs over the Pacific and Atlantic Oceans were consistent (Fig. 4c, d). The regional mean differences between the two oceans were because of the dipole spatial patterns in energy budget terms (Fig. 4c, d). For the two oceans, the positive changes in the latent heat in the north and net shortwave radiation in the south were dominant factors causing the enhanced atmospheric energy inputs to oceans (Fig. 4c, d). The longwave radiation and sensible heat also had positive contributions in the north but in smaller magnitudes and areas.

The air-sea interactions underlying the shortwave radiation and air-sea latent heat flux changes over the two oceans were elucidated as follows. The increased net shortwave radiation in the south was induced by an increase in downward shortwave radiation (Fig. S12 online), which was because of the sinking motion-induced reduction in clouds (Fig. 5a–c). The sinking motion was caused by the TP heating-induced horizontal heat transport and barotropic high-pressure circulation anomalies, as shown in Section 3.1. Given that the air-sea interactions amplified the subtropical westward and extratropical eastward belts of the horizontal heat flux across the Northern Hemisphere (Fig. 1c and Fig. S7a online), the barotropic circulation development and pertinent sinking motion were also enhanced.

The positive changes in latent heat in the north (Fig. 4c, d) correspond to the decrease in upward air-sea latent heat flux and less evaporation at the sea surface. The latent heat flux and evaporation are proportional to the air-sea humidity difference and near-surface wind speed according to bulk parameterizations (Section 2.4). The air-sea humidity difference decreased in the north over the two oceans (Fig. 5d), favoring the decrease in air-sea latent heat flux. In contrast, the near-surface wind speed increased in the north (Fig. S13c online), which favored an increase in air-sea latent heat flux. The air-sea humidity difference decreased because the specific humidity of the near-surface air increased more than the saturation specific humidity at the sea surface (Fig. S13a, b online). The increase in specific humidity of the near-surface air was favored by the moisture convergence in the north and enhanced moisture source from the sea surface in the south (Fig. S14 online), respectively. The moisture convergence in the north further links to the enhanced moisture transport along the northward pathway in Fig. 1d, which was amplified by the air-sea interactions (Fig. S7b online). Therefore, the enhanced moisture transport from air-sea interactions and corresponding decreased air-sea humidity difference was responsible for the decrease in air-sea latent heat flux in the north of the two oceans.

In summary (Fig. 6), horizontal heat and moisture transport and pertinent atmospheric circulations, including disturbances in westerlies, stationary wave trains, and zonal-vertical cells, triggered the changes over the North Pacific and Atlantic Oceans. In turn, the air-sea interactions amplified the pathways in horizontal heat/moisture transport and atmospheric circulations. The key local feedback processes were associated with the air-sea latent heat flux and the sinking motion-induced cloud and shortwave radiation over the Pacific and Atlantic Oceans. Given that air-sea

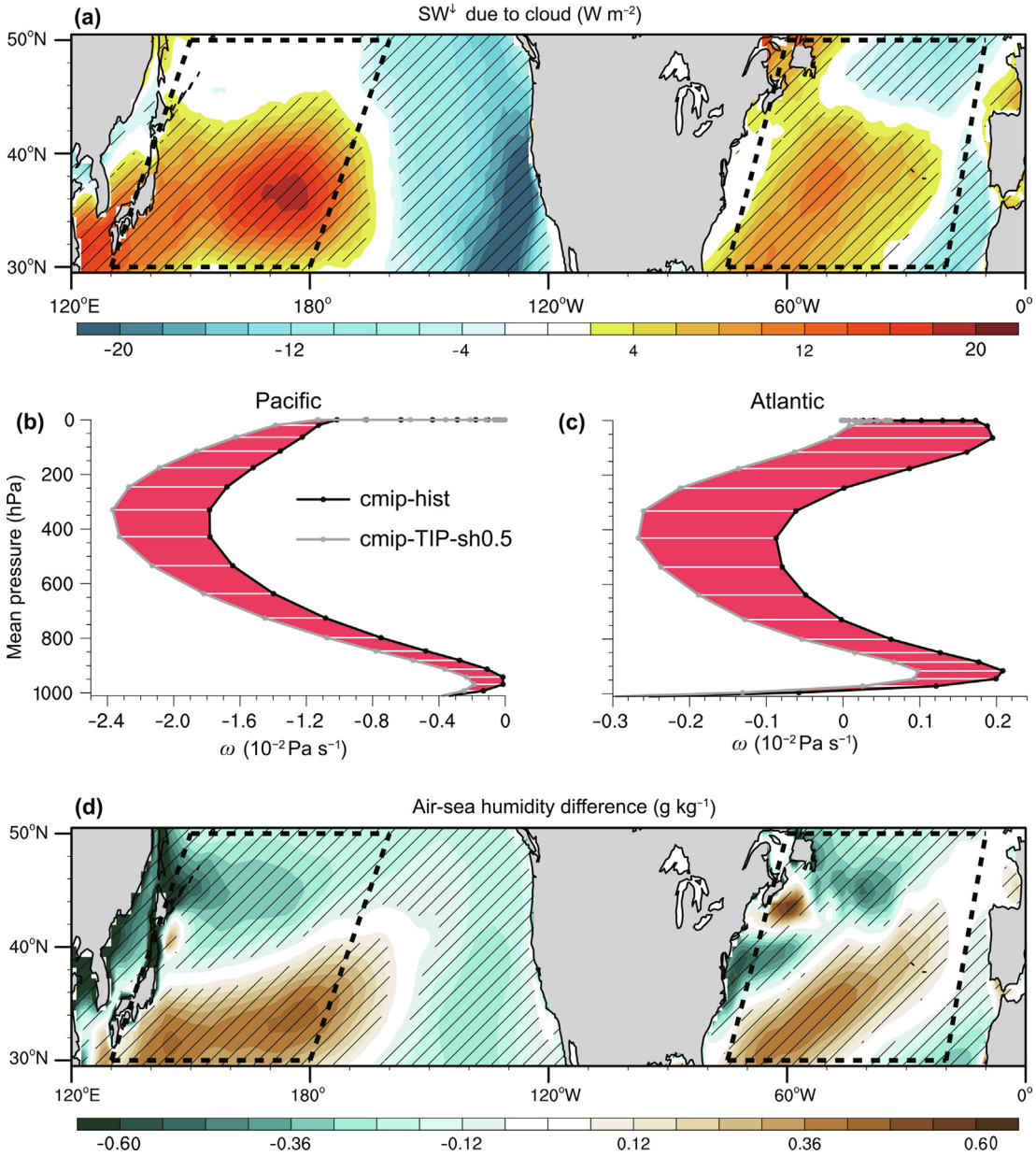

Fig. 5. Causes of the changes in net shortwave radiation and air-sea latent heat flux. (a) Differences in JJA mean downward shortwave radiation ($SW^{\downarrow}$) from cloud calculated as downward shortwave radiation minus its clear-sky values, determined using cmip-hist minus cmip-TIP-sh0.5 experiments for 1850–2014. The dashed polygons indicate Pacific and Atlantic domains. (b), (c) Regional mean vertical velocity (ω) averaged over the Pacific and Atlantic domains with positive values in (a) for cmip-hist and cmip-TIP-sh0.5 experiments, respectively. The red shading indicates that differences using the cmip-hist minus cmip-TIP-sh0.5 are positive, namely an enhanced sinking motion. (d) Same as (a) but for air-sea humidity difference (Section 2.4). The stripe indicates significant differences at the 95% confidence level.

interactions over the Indian Ocean partially offset the direct meridional-vertical cell induced by TP heating [30], the Indian Ocean does not act as an oceanic repeater but changes the patterns of the response to TP heating. Specifically, in response to the sinking motion, the air-sea interactions over the Indian Ocean reversely stimulated the ascending motion over a small region (Fig. S6i online) [30], while the air-sea interactions over the North Pacific and Atlantic Oceans further favored the TP heating-induced sinking motion (Fig. 5). Nonetheless, the fundamental factors, such as the distinct latitudinal locations, that determined the different effects of air-sea interactions over the tropical Indian Ocean and extratropical Pacific and Atlantic Oceans still require further investigations. Therefore, the North Pacific and Atlantic Oceans are two prominent oceanic repeaters that amplify the global climate effect of TP heating.

4. Discussion and conclusions

This study demonstrated the robust effect of TP heating on the global climate beyond Asian monsoon regions and highlighted the key role of oceanic repeaters. The regions under the influence of TP heating, pertinent atmospheric pathways, and air-sea interactions associated with Pacific and Atlantic oceanic repeaters are summarized in Fig. 6. Given that previous studies have focused on Asian monsoon regions or paleoclimate, our study showed that the anomalous TP heating within the current climate variability range can induce significant climate responses over many regions globally under a fixed modern TP topography. The high response-to-forcing ratio because of oceanic repeaters implies that TP heating may efficiently modulate current climate variability. Our findings extend the prior understanding of the climate effect of TP uplift

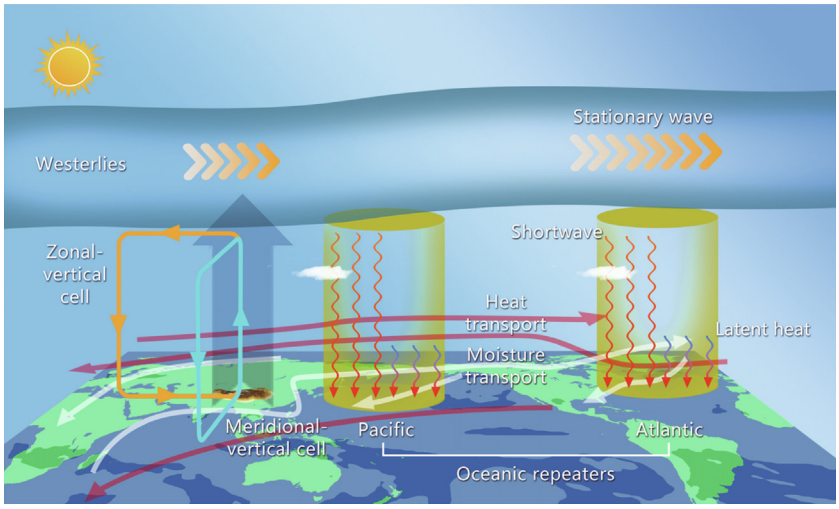

Fig. 6. Schematic view of the climate effect of TP heating and pertinent air-sea interactions of Pacific and Atlantic oceanic repeaters. Transparent white shading indicates the regions where the temperature or precipitation is significantly influenced by TP heating in summer, namely the regions where the differences in temperature or precipitation between cmip-hist and cmip-TIP-sh0.5 experiments were significant at the 95% confidence level (Fig. S6 online). The pathways of horizontal heat and moisture transport and atmospheric circulations and the dominant local air-sea feedback processes are illustrated. The cyan color of the meridional-vertical cell indicates that air-sea interactions have no amplification effect, whereas the warm color or transparency indicates that air-sea interactions amplify the pertinent pathways.

on paleoclimate evolution [4–17] to the current climate variability. Consequently, further research into TP heating-modulated air-sea interactions is necessary for a better comprehension of the current climate change.

In addition to the air-sea interactions triggered by TP heating we identified, oceans have inherent variability modes. The interdecadal Pacific oscillation [59,60] and El Niño/La Niña [61,62] are prominent modes in the Pacific, and the Atlantic multidecadal oscillation [63,64] is a prominent mode in the Atlantic. How these oceanic modes reversely influence TP heating should also be investigated. Atlantic variability can regulate the influence of TP heating on the climate of its upstream regions [32]. However, a detailed understanding of the two-way interactions between TP heating and typical oceanic modes and further modulations of the global climate requires further investigation. Furthermore, given that there are potential interactions between the thermal and mechanical effects of the TP [65], the thermal and dynamic interactions in our simulations should be investigated further. During the past two millennia, the current TP warming is likely unprecedented [66–68]. The TP temperature and sensible heating are also projected to increase continuously in the future based on multimodel simulations [69,70]. Consequently, it is anticipated that our findings will stimulate research into the effects of two-way interactions between TP heating and oceanic modes on future climate change.

Conflict of interest

The authors declare that they have no conflict of interest.

Acknowledgments

This work was supported by the National Natural Science Foundation of China (91937302), the Fundamental Research Funds for the Central Universities (lzujbky-2022-kb10), and the Gansu Provincial Special Fund Project for Guiding Scientific and Technological Innovation and Development (2019ZX-06). We thank the anonymous reviewers for their constructive comments. We thank Zhaoyi Shen at California Institute of Technology and Yi Ming at Boston College for their comments. We acknowledge the CMIP Panel and WCRP's Working Group on Coupled Modelling for maintaining GMMIP data. We are also grateful to the institutes for sharing their model output. We thank the CESM Working Groups NCAR/UCAR for providing the CESM-2.1.3 model and the National Supercomputing Center in Wuxi, China for providing technical support during CESM-2.1.3 porting. We also thank the NCEP/DOE, ECMWF, NASA/GISS, and NOAA/OAR/ESRL PSL for making their data available.

Author contributions

Jianping Huang, Guoxiong Wu, and Yongkun Xie provided the initial concept of this research. Guoxiong Wu, Jianping Huang, and Yongkun Xie designed the research proposal and developed the technical route. Yongkun Xie performed numerical simulations, data processing, and plotting. All authors contributed to the analyses of the results, manuscript writing, and all stages of revision.

Appendix A. Supplementary materials

Supplementary materials to this article can be found online at https://doi.org/10.1016/j.scib.2023.07.019.

References

[1] Blanford H. On the connexion of the Himalayan snowfall with dry winds and seasons of droughts in India. Proc R Soc Lond 1884;37:3–22.
[2] Queney P. The problem of air flow over mountains: a summary of theoretical studies. Bull Am Meteorol Soc 1948;29:16–26.
[3] Yeh T-C. The circulation of the high troposphere over China in the winter of 1945–46. Tellus 1950;2:173–83.
[4] Manabe S, Terpstra T. The effects of mountains on the general circulation of the atmosphere as identified by numerical experiments. J Atmos Sci 1974;31:3–42.
[5] Hahn D, Manabe S. The role of mountains in the South Asian monsoon circulation. J Atmos Sci 1975;32:1515–41.
[6] Manabe S, Broccoli A. Mountains and arid climates of middle latitudes. Science 1990;247:192–5.
[7] Ruddiman W, Kutzbach J. Forcing of late Cenozoic northern hemisphere climate by plateau uplift in southern Asia and the American west. J Geophys Res-Atmos 1989;94:18409–27.
[8] Molnar P, England P, Martinod J. Mantle dynamics, uplift of the Tibetan Plateau, and the Indian Monsoon. Rev Geophys 1993;31:357–96.
[9] An Z, Kutzbach J, Prell W, et al. Evolution of Asian monsoons and phased uplift of the Himalay-Tibetan plateau since Late Miocene times. Nature 2001;411:62–6.

[10] Kutzbach J, Prell W, Ruddiman W. Sensitivity of Eurasian climate to surface uplift of the Tibetan Plateau. J Geol 1993;101:177–90.
[11] Kitoh A. Mountain uplift and surface temperature changes. Geophys Res Lett 1997;24:185–8.
[12] Kitoh A. Effects of large-scale mountains on surface climate—a coupled ocean–atmosphere general circulation model study. J Meteorol Soc Jpn 2002;80:1165–81.
[13] Kitoh A. Effects of mountain uplift on East Asian summer climate investigated by a coupled atmosphere–ocean GCM. J Clim 2004;17:783–802.
[14] Fallah B, Cubasch U, Prömmel K, et al. A numerical model study on the behaviour of Asian summer monsoon and AMOC due to orographic forcing of Tibetan Plateau. Clim Dyn 2016;47:1485–95.
[15] Su B, Jiang D, Zhang R, et al. Difference between the North Atlantic and Pacific meridional overturning circulation in response to the uplift of the Tibetan Plateau. Clim Past 2018;14:751–62.
[16] Yang H, Shen X, Yao J, et al. Portraying the impact of the Tibetan Plateau on global climate. J Clim 2020;33:3565–83.
[17] Ferreira D, Cessi P, Coxall H, et al. Atlantic-Pacific asymmetry in deep water formation. Annu Rev Earth Planet Sci 2018;46:327–52.
[18] Yanai M, Li C, Song Z. Seasonal heating of the Tibetan Plateau and its effects on the evolution of the Asian summer monsoon. J Meteorol Soc Jpn 1992;70:319–51.
[19] Liu Y, Wu G, Hong J, et al. Revisiting Asian monsoon formation and change associated with Tibetan Plateau forcing: II. change. Clim Dyn 2012;39:1183–95.
[20] Held I, Ting M. Orographic versus thermal forcing of stationary waves: the importance of the mean low-level wind. J Atmos Sci 1990;47:495–500.
[21] Held I, Ting M, Wang H. Northern winter stationary waves: theory and modeling. J Clim 2002;15:2125–44.
[22] Wu G, Liu Y, Zhang Q, et al. The influence of mechanical and thermal forcing by the Tibetan Plateau on Asian climate. J Hydrometeorol 2007;8:770–89.
[23] Boos W, Kuang Z. Dominant control of the South Asian monsoon by orographic insulation versus plateau heating. Nature 2010;463:218–22.
[24] Son J, Seo K, Wang B. Dynamical control of the Tibetan Plateau on the East Asian summer monsoon. Geophys Res Lett 2019;46:7672–9.
[25] Wu G, Liu Y, He B, et al. Thermal controls on the Asian summer monsoon. Sci Rep 2012;2:404.
[26] Wang B, Bao Q, Hoskins B, et al. Tibetan Plateau warming and precipitation changes in East Asia. Geophys Res Lett 2008;35:L14702.
[27] He B, Wu G, Liu Y, et al. Astronomical and hydrological perspective of mountain impacts on the Asian summer monsoon. Sci Rep 2015;5:17586.
[28] Yanai M, Wu G. Effects of the Tibetan Plateau. In: Wang B, editor. The Asian monsoon. Springer Praxis Books. Berlin, Heidelberg: Springer; 2006.
[29] Baldwin J, Vecchi G, Bordoni S. The direct and ocean-mediated influence of Asian orography on tropical precipitation and cyclones. Clim Dyn 2019;53:805–24.
[30] He B, Liu Y, Wu G, et al. The role of air-sea interactions in regulating the thermal effect of the Tibetan Iranian Plateau on the Asian summer monsoon. Clim Dyn 2019;52:4227–45.
[31] Sun R, Duan A, Chen L, et al. Interannual variability of the North Pacific mixed layer associated with the spring Tibetan Plateau thermal forcing. J Clim 2019;32:3109–30.
[32] Lu M, Huang B, Li Z, et al. Role of Atlantic air-sea interaction in modulating the effect of Tibetan Plateau heating on the upstream climate over Afro-Eurasia-Atlantic regions. Clim Dyn 2019;53:509–19.
[33] Lu M, Yang S, Wang J, et al. Response of regional Asian summer monsoons to the effect of reduced surface albedo in different Tibetan Plateau domains in idealized model experiments. J Clim 2021;34:7023–36.
[34] Lu M, Yang S, Li Z, et al. Possible effect of the Tibetan Plateau on the "upstream" climate over West Asia, North Africa, South Europe and the North Atlantic. Clim Dyn 2018;51:1485–98.
[35] Zhou T, Turner A, Kinter J, et al. GMMIP (v1.0) contribution to CMIP6: global monsoons model inter-comparison project. Geosci Model Dev 2016;9:3589–604.
[36] Adler R, Huffman G, Chang A, et al. The version 2 global precipitation climatology project (GPCP) monthly precipitation analysis (1979–present). J Hydrometeorol 2003;4:1147–67.
[37] Lenssen N, Schmidt G, Hansen J, et al. Improvements in the GISTEMP uncertainty model. J Geophys Res-Atmos 2019;124:6307–26.
[38] Hersbach H, Bell B, Berrisford P, et al. The ERA5 global reanalysis. Q J R Meteorol Soc 2020;146:1999–2049.
[39] Kanamitsu M, Ebisuzaki W, Woollen J, et al. NCEP-DOE AMIP-II reanalysis (R-2). Bull Am Meteorol Soc 2002;83:1631–43.
[40] Eyring V, Bony S, Meehl G, et al. Overview of the coupled model intercomparison project phase 6 (CMIP6) experimental design and organization. Geosci Model Dev 2016;9:1937–58.
[41] He B, Liu Y, Wu G, et al. CAS FGOALS-f3-L model datasets for CMIP6 GMMIP Tier-1 and Tier-3 experiments. Adv Atmos Sci 2020;37:18–28.
[42] Bao Y, Song Z, Qiao F. FIO-ESM version 2.0: model description and evaluation. J Geophys Res-Oceans 2020;125:e2019JC016036.
[43] Danabasoglu G, Lamarque J, Bacmeister J, et al. The community Earth system model version 2 (CESM2). J Adv Model Earth Syst 2020;12:e2019MS001916.
[44] Laguë M, Bonan G, Swann A. Separating the impact of individual land surface properties on the terrestrial surface energy budget in both the coupled and uncoupled land–atmosphere system. J Clim 2019;32:5725–44.
[45] Xie Y, Wu G, Liu Y, et al. A potential vorticity budget view of the atmospheric circulation climatology over the Tibetan Plateau. Int J Climatol 2023;43:2031–49.
[46] Paulson C, Simpson J. Irradiance measurements in the upper ocean. J Phys Oceanogr 1977;7:952–6.
[47] Zhang M. NUMERICAL MODELS | Coupled ocean-atmosphere models: physical processes. In: North GR, Pyle JA, Zhang FQ, editors. Encyclopedia of atmospheric sciences. London: Academic Press; 2015. p. 144–52.
[48] Wallace J, Hobbs P. Atmospheric Science: an introductory survey. 2nd ed. London: Academic Press; 2006. p. 504.
[49] Huang J. A simple accurate formula for calculating saturation vapor pressure of water and ice. J Appl Meteorol Climatol 2018;57:1265–72.
[50] Rodwell M, Hoskins B. Monsoons and the dynamics of deserts. Q J R Meteorol Soc 1996;122:1385–404.
[51] Liu Y, Wang Z, Zhuo H, et al. Two types of summertime heating over Asian large-scale orography and excitation of potential-vorticity forcing II. Sensible heating over Tibetan-Iranian Plateau. Sci China Earth Sci 2017;60:733–44.
[52] Nan S, Zhao P, Chen J. Variability of summertime Tibetan tropospheric temperature and associated precipitation anomalies over the central-eastern Sahel. Clim Dyn 2019;52:1819–35.
[53] Plumb R, Hou A. The response of a zonally symmetric atmosphere to subtropical thermal forcing: threshold behavior. J Atmos Sci 1992;49:1790–9.
[54] Wu G, Zhuo H, Wang Z, et al. Two types of summertime heating over the Asian large-scale orography and excitation of potential-vorticity forcing I. Over Tibetan Plateau. Sci China Earth Sci 2016;59:1996–2008.
[55] Kawamura R. A possible mechanism of the Asian summer monsoon-ENSO coupling. J Meteorol Soc Jpn 1998;76:1009–27.
[56] Smagorinsky J. The dynamical influence of large scale heat sources and sinks on the quasi-stationary mean motions of the atmosphere. Q J R Meteorol Soc 1953;79:342–66.
[57] Wu G, He B, Liu Y, et al. Location and variation of the summertime upper-troposphere temperature maximum over South Asia. Clim Dyn 2015;45:2757–74.
[58] Wang L, Yang H, Wen Q, et al. Tibetan Plateau's far-reaching impacts on Arctic and Antarctic climate: seasonality and pathways. J Clim 2023;36:1399–414.
[59] Meehl G, Teng H, Arblaster J. Climate model simulations of the observed early-2000s hiatus of global warming. Nat Clim Chang 2014;4:898–902.
[60] Huang J, Xie Y, Guan X, et al. The dynamics of the warming hiatus over the Northern Hemisphere. Clim Dyn 2017;48:429–46.
[61] Wang B, An S-I. A mechanism for decadal changes of ENSO behavior: roles of background wind changes. Clim Dyn 2002;18:475–86.
[62] Kosaka Y, Xie S. Recent global-warming hiatus tied to equatorial Pacific surface cooling. Nature 2013;501:403–7.
[63] Tung K, Zhou J. Using data to attribute episodes of warming and cooling in instrumental records. Proc Natl Acad Sci USA 2013;110:2058–63.
[64] Chen X, Tung K. Varying planetary heat sink led to global-warming slowdown and acceleration. Science 2014;345:897–903.
[65] Wu G. The nonlinear response of the atmosphere to large-scale mechanical and thermal forcing. J Atmos Sci 1984;41:2456–76.
[66] Yao T, Xue Y, Chen D, et al. Recent third pole's rapid warming accompanies cryospheric melt and water cycle intensification and interactions between monsoon and environment: multidisciplinary approach with observations, modeling, and analysis. Bull Am Meteorol Soc 2019;100:423–44.
[67] Chen F, Ding L, Piao S, et al. The Tibetan Plateau as the engine for Asian environmental change: the Tibetan Plateau Earth system research into a new era. Sci Bull 2021;66:1263–6.
[68] Guo D, Pepin N, Yang K, et al. Local changes in snow depth dominate the evolving pattern of elevation-dependent warming on the Tibetan Plateau. Sci Bull 2021;66:1146–50.
[69] You Q, Cai Z, Pepin N, et al. Warming amplification over the Arctic Pole and Third Pole: trends, mechanisms and consequences. Earth Sci Rev 2021;217:103625.
[70] Wang M, Wang J, Chen D, et al. Recent recovery of the boreal spring sensible heating over the Tibetan Plateau will continue in CMIP6 future projections. Environ Res Lett 2019;14:124066.

Yongkun Xie is a research scientist at Lanzhou University's Collaborative Innovation Center for Western Ecological Safety. In 2017, he earned his doctorate from Lanzhou University. His research interest includes climate dynamics and change pertaining to the Tibetan Plateau, Arctic, and dryland.

Jianping Huang is an academician of the Chinese Academy of Sciences, a distinguished professor and founder of the College of Atmospheric Sciences at Lanzhou University. In 1988, he obtained his doctorate from Lanzhou University. His research focuses on the monitoring and prediction of dust storms and semi-arid climate change. In recent years, his team has pioneered the study of the oxygen cycle.

Guoxiong Wu is an academician and life tenure professor of the Chinese Academy of Sciences, International Science Council fellow, and American Geophysical Union fellow. In 1983, he obtained his Ph.D. degree from Imperial College London. His research interest includes the climate dynamics of the Tibetan Plateau, the land-air-sea interactions of the Asian monsoon, and subtropical weather and climate dynamics.

Supplementary Materials

Oceanic repeaters boost the global climatic impact of the Tibetan Plateau

Yongkun Xie[a], Jianping Huang[a]*, Guoxiong Wu[b,c]*, Yimin Liu[b,c], Wenhao Dong[d,e], Mengmeng Lu[f,g], Bian He[b,c], Zifan Su[a,h], Qing Bao[b,c], Qingyun Zhao[a], Yuzhi Liu[a]

Contents:

[a] Collaborative Innovation Center for Western Ecological Safety, Lanzhou University, Lanzhou, China
[b] State Key Laboratory of Numerical Modeling for Atmospheric Sciences and Geophysical Fluid Dynamics (LASG), Institute of Atmospheric Physics, Chinese Academy of Sciences, Beijing, China
[c] College of Earth and Planetary Sciences, University of Chinese Academy of Sciences, Beijing, China
[d] NOAA/Geophysical Fluid Dynamics Laboratory, Princeton, NJ, USA
[e] Cooperative Programs for the Advancement of Earth System Science, University Corporation for Atmospheric Research, Boulder, CO, USA
[f] State Key Laboratory of Severe Weather and Institute of Climate System, Chinese Academy of Meteorological Sciences, Beijing, China
[g] Southern Marine Science and Engineering Guangdong Laboratory (Zhuhai), Zhuhai, China
[h] College of Atmospheric Sciences, Lanzhou University, Lanzhou, China.
* Corresponding author: Jianping Huang, hjp@lzu.edu.cn; Guoxiong Wu, gxwu@lasg.iap.ac.cn

Supplementary Data and methods

1. GPCP

The Global Precipitation Climatology Project (GPCP), version 2.3, dataset has a resolution of 2.5° × 2.5° and is available for the period ranging from January 1979 to the present. The GPCP is provided by NOAA/OAR/ESRL PSL, Boulder, Colorado, USA and can be accessed from https://psl.noaa.gov/data/gridded/data.gpcp.html.

2. GISTEMP

The Goddard Institute for Space Studies (GISS) Surface Temperature Analysis (GISTEMP), version 4, dataset has a resolution of 2° × 2° and is available for the period ranging from January 1880 to the present. The GISTEMP is provided by NASA/GISS and can be accessed from https://data.giss.nasa.gov/gistemp/.

3. ERA5

The fifth-generation ECMWF reanalysis dataset (ERA5) is the latest version of the ECMWF reanalysis and is available for the period ranging from January 1950 to the present, wherein single-level surface data were used. ERA5 data are in monthly mean and have a resolution of 1° × 1°. The variables examined were 2 m air temperature. ERA5 data can be accessed at the ECMWF website https://www.ecmwf.int/en/forecasts/datasets/reanalysis-datasets/era5.

4. NCEP-2

NCEP-DOE Reanalysis-2 (NCEP-2) monthly sigma-level fields of diabatic heating of the atmosphere provide six separate components of diabatic heating, which allowed us to examine the individual physical processes contributing to total diabatic heating. The six physical process-based components were solar and longwave radiative, vertical diffusion (sensible heat), large-scale condensation, and deep and shallow convective heat. NCEP-2 is in a global T62 Gaussian grid with 28 vertical sigma levels, available for the period ranging from January 1979 to August 2014. NCEP-2 data can be accessed at http://iridl.ldeo.columbia.edu/SOURCES/.NOAA/.NCEP-DOE/.Reanalysis-2/.Monthly/.dg3/.dg3/.

5. Numerical simulations

GMMIP officially proposed six experiments, two of which were useful for our study—amip-hist and amip-TIP-nosh (Table S1). Among all the models that participated in GMMIP, only two, i.e., FGOALS-f3-L and FIO-ESM-2-0, had all the outputs of the three required experiments available. GMMIP data are available to the public on the CMIP6 website: https://esgf-node.llnl.gov/search/cmip6/.

6. Statistical significance of the difference and correlation

To determine the statistical significance (95% confidence level) of the difference between the control and sensitivity runs, a two-tailed Student's *t*-test was performed. The function of the *t*-test is documented on the NCL website https://www.ncl.ucar.edu/Document/Functions/Built-in/ttest.shtml. The statistical significance (95% confidence level) of the correlation coefficient was determined using a two-tailed Pearson's *r*-test. The function used to calculate the correlation coefficient is documented at https://www.ncl.ucar.edu/Document/Functions/Built-in/escorc.shtml, while the function of the *r*-test is documented at https://www.ncl.ucar.edu/Document/Functions/Built-in/rtest.shtml.

Supplementary Figures S1–S14

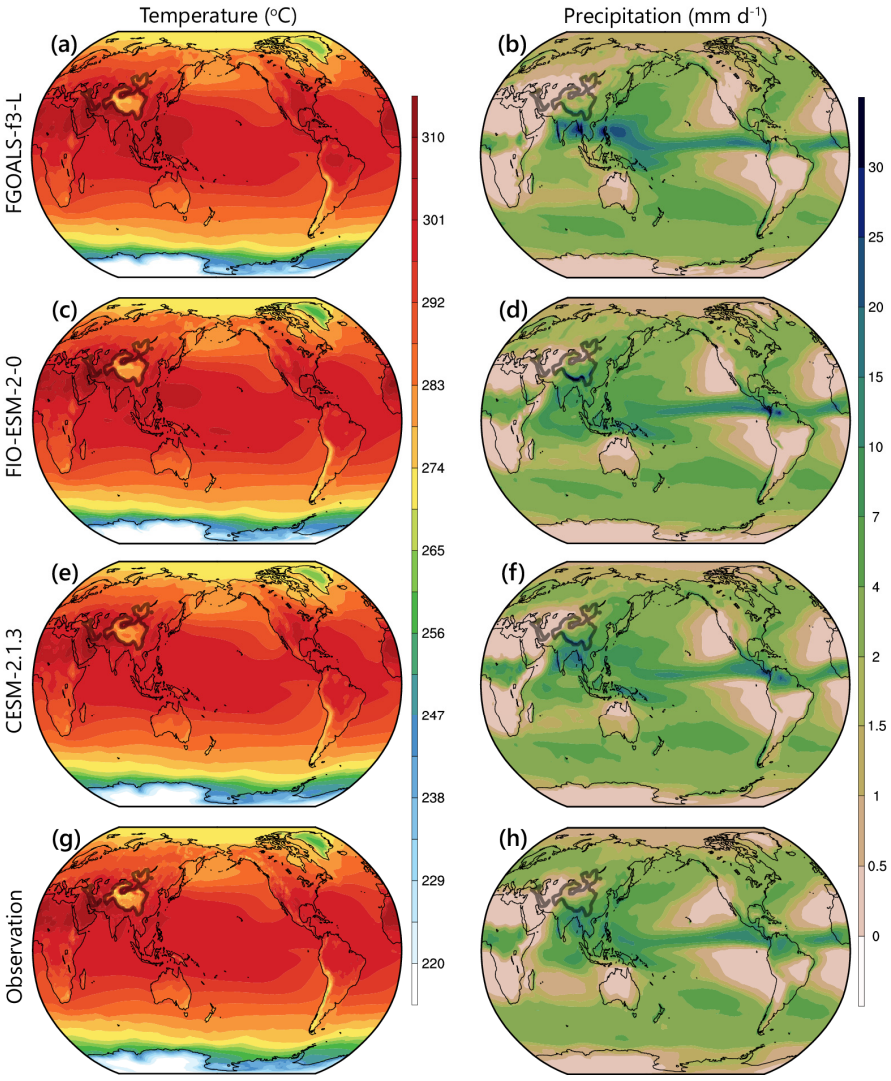

Fig. S1. Climatology of the June to August (JJA) mean temperature and precipitation. Near-surface air temperature and precipitation averaged from 1979–2014 based on amip-hist experiment of (a, b) FGOALS-f3-L, (c, d) FIO-ESM-2-0, and (e, f) CESM-2.1.3 models and from observational data of (g) ERA5 and (h) GPCP. The thick grey contour indicates 1.5 km elevation.

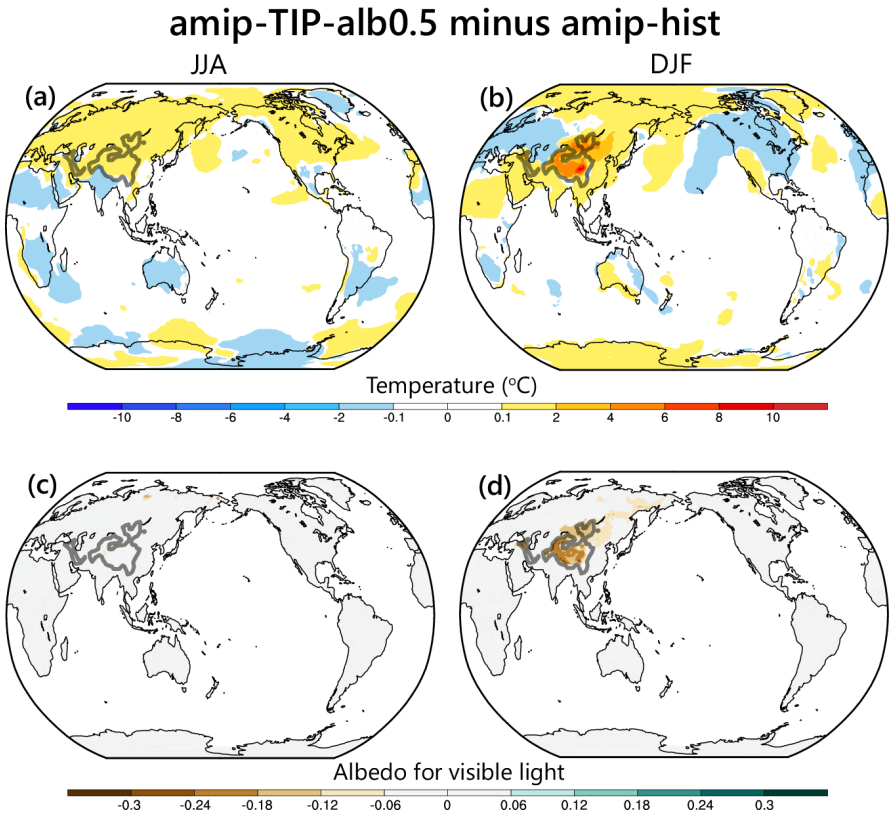

Fig. S2. Spatial pattern of anomalous TP heating in the half-albedo experiment. Differences in JJA and DJF mean (a, b) near-surface air temperature and (c, d) albedo for visible light determined using amip-TIP-alb0.5 minus amip-hist for 1979–2014. The thick grey contour indicates 1.5 km elevation.

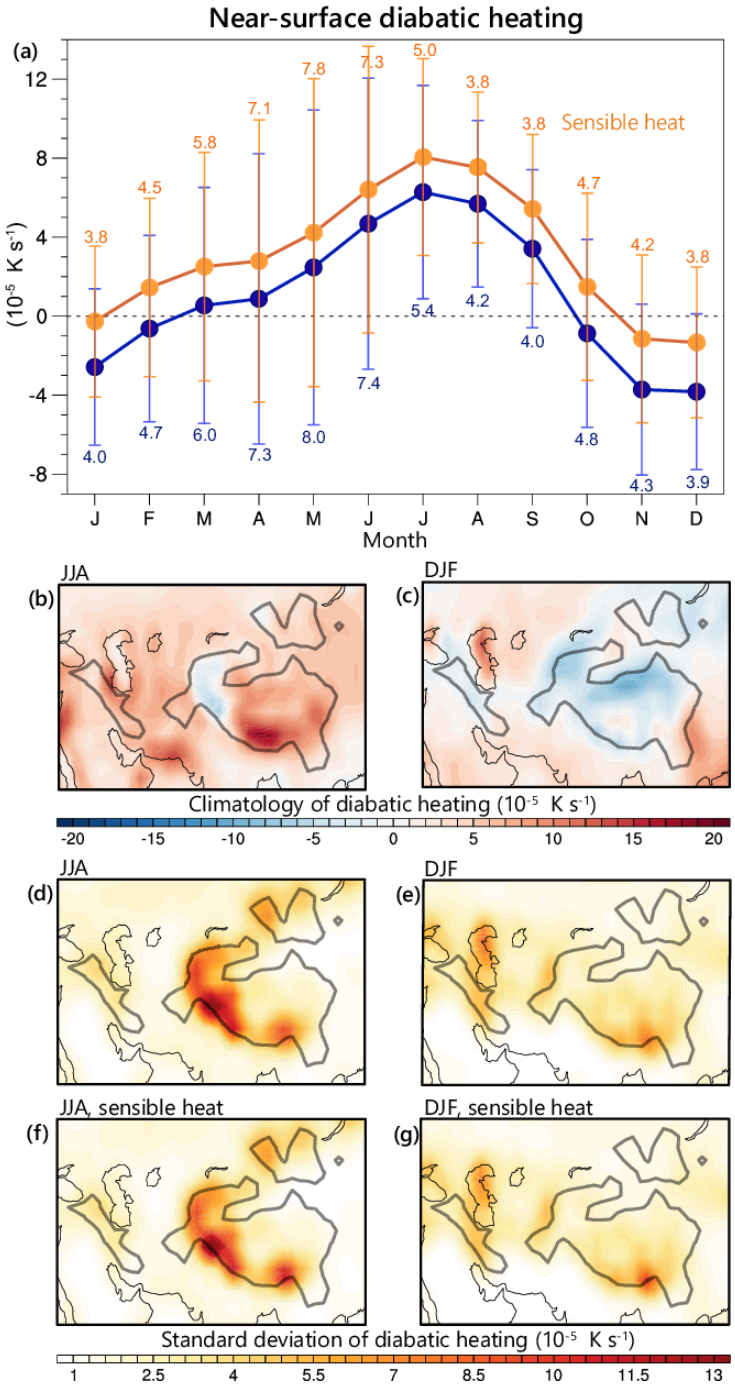

Fig. S3. Seasonality and patterns of TP heating. (a) Monthly mean diabatic heating at 0.995 sigma level (blue) and its component contributed by sensible heat (orange), averaged over the TP domain higher than 1.5 km from NCEP-2 data, for 1979–2014. The vertical bar indicates the range of one standard deviation (number). (b), (c) Spatial patterns of the climatological diabatic heating in JJA and DJF. (d), (e) Spatial patterns of the standard deviation of diabatic heating in JJA and DJF. (f, g) Same as (d, e) but for the sensible heat component. The thick grey contour indicates 1.5 km elevation.

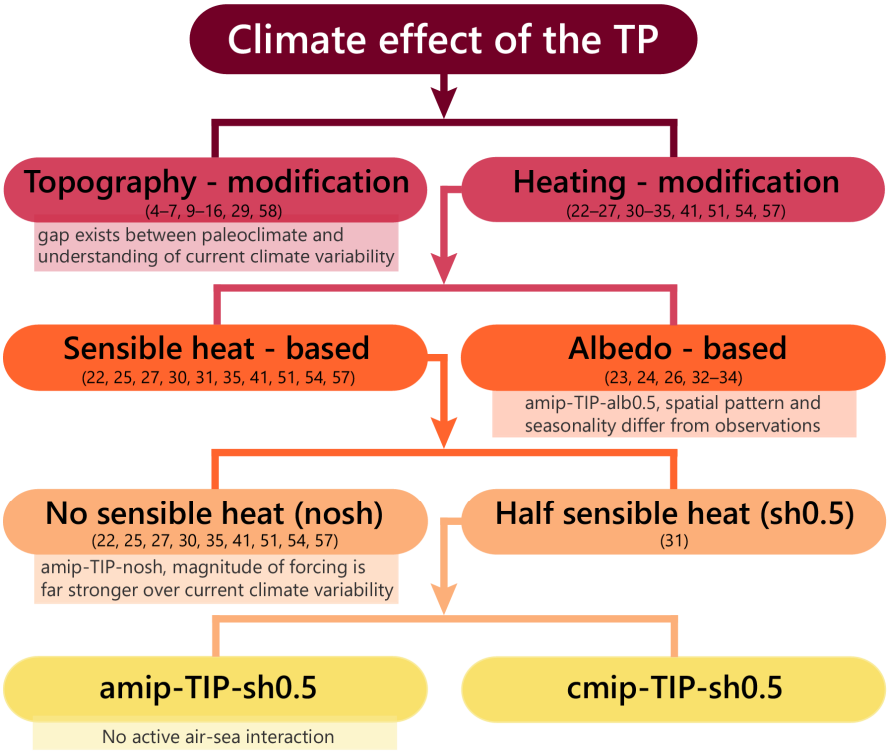

Fig. S4. Schematic summary of the categories of experimental designs used for simulating the climate effect of the TP. Limitations of the experiments in terms of our research purpose are noted in the drop-down panel. The previous studies that have used each experimental design are also marked.

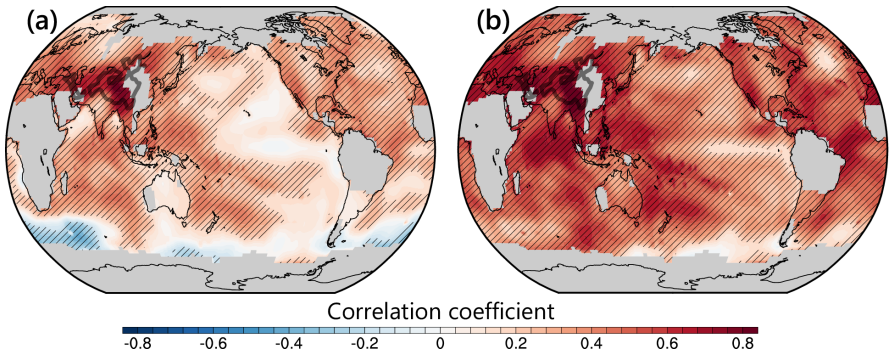

Fig. S5. The correlation of the TP temperature with the global temperature. (a) The correlation coefficient between the JJA mean near-surface air temperature averaged over the TP domain higher than 1.5 km with global near-surface air temperature after linear detrending for 1880–2022, based on GISTEMP data. (b) Same as (a) but for result without linear detrending. The stripe indicates significant correlation at the 95% confidence level. The grey filling indicates the missing value in GISTEMP data. The thick grey contour indicates 1.5 km elevation.

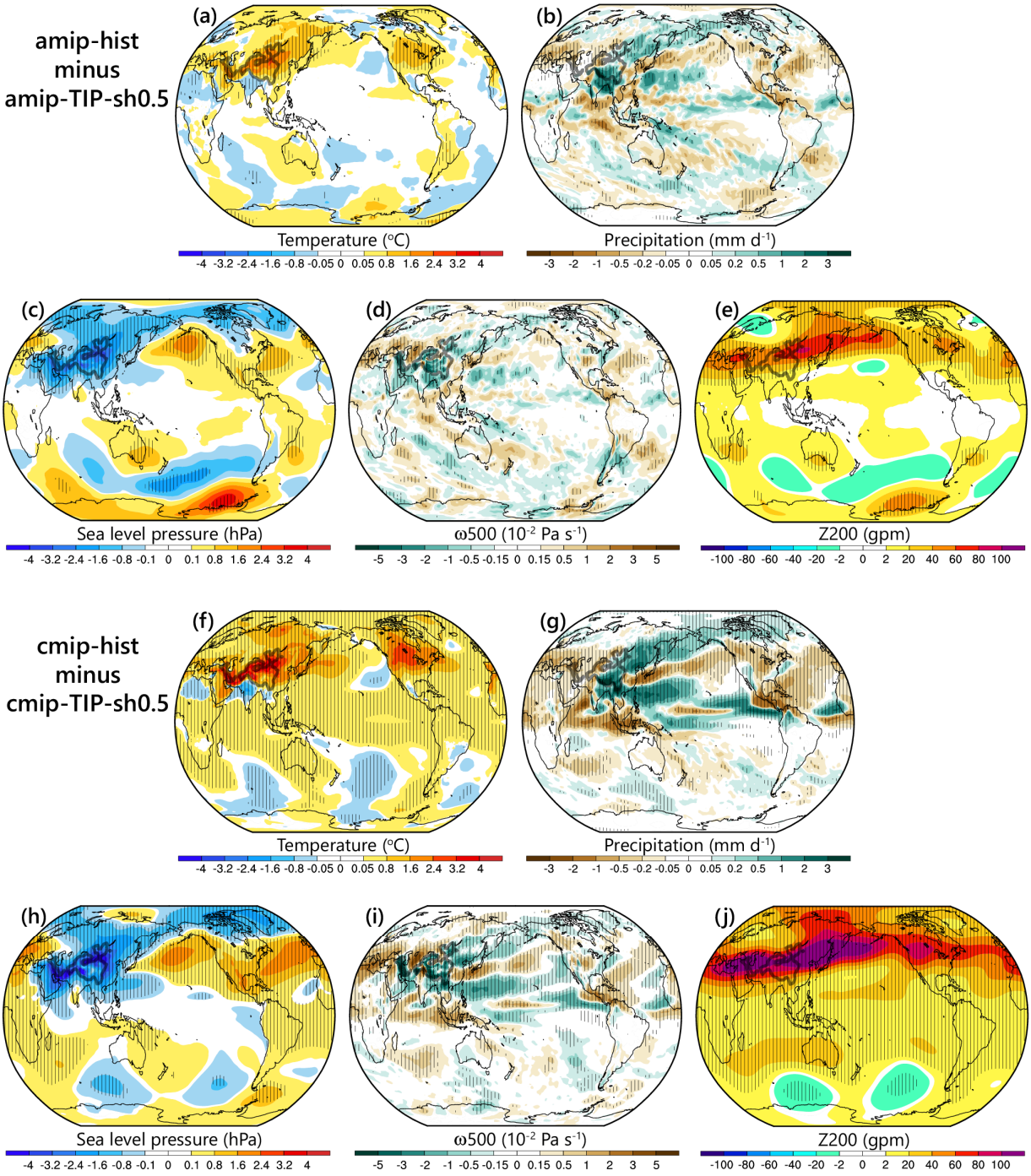

Fig. S6. Impact of TP heating on global climate in summer in amip and cmip experiments. Differences in JJA mean (a) near-surface air temperature, (b) precipitation, (c) sea level pressure, (d) ω500, and (e) Z200 determined using amip-hist minus amip-TIP-sh0.5 for 1979–2014. (f–j) Same as (a–e) but for cmip-hist minus cmip-TIP-sh0.5 for 1850–2014. The stripe indicates significant differences at the 95% confidence level. The thick grey contour indicates 1.5 km elevation.

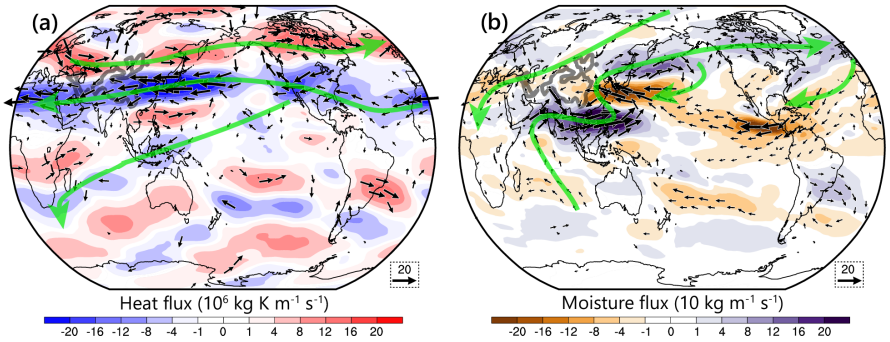

Fig. S7. Impact of air-sea interactions on horizontal heat and moisture transport. Differences in JJA mean vertically-integrated horizontal (a) heat and (b) moisture flux (vector) and their zonal components (color shading) determined using cmip (cmip-hist minus cmip-TIP-sh0.5) minus amip (amip-hist minus amip-TIP-sh0.5) experiments for 2000–2014. The vectors with insignificant (95% confidence level) differences in both zonal and meridional components were not shown; the green arrows indicate the pathways of heat or moisture flux. The thick grey contour indicates 1.5 km elevation.

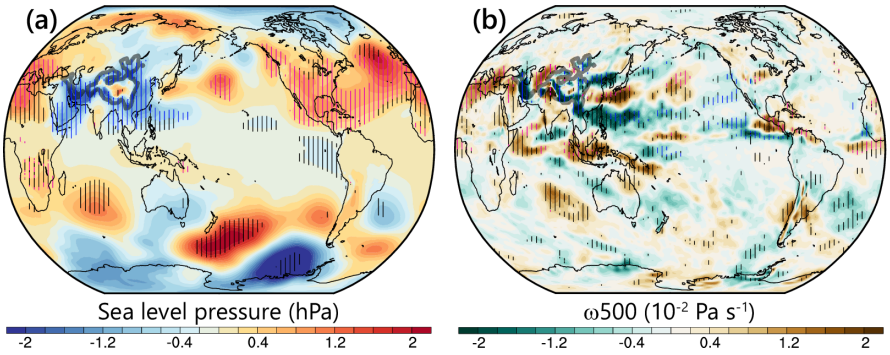

Fig. S8. Effect of air-sea interactions on sea level pressure and vertical motion. Differences in JJA mean (a) sea level pressure and (b) ω500 determined using cmip (cmip-hist minus cmip-TIP-sh0.5) minus amip (amip-hist minus amip-TIP-sh0.5) experiments for 1850–2014. The stripe indicates significant differences in cmip minus amip at the 95% confidence level; the red and blue colors further indicate all-positive and all-negative configurations in the signs of cmip, amip, and cmip minus amip. The thick grey contour indicates 1.5 km elevation.

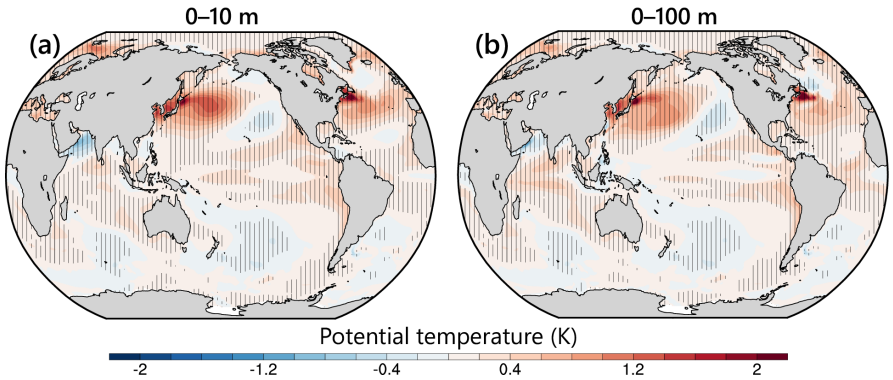

Fig. S9. Impact of TP heating on subsurface ocean temperature in summer. Differences in JJA mean subsurface ocean potential temperature for (a) 0–10 m and (b) 0–100 m layers determined using cmip-hist minus cmip-TIP-sh0.5 for 1850–2014. The stripe indicates significant differences at the 95% confidence level.

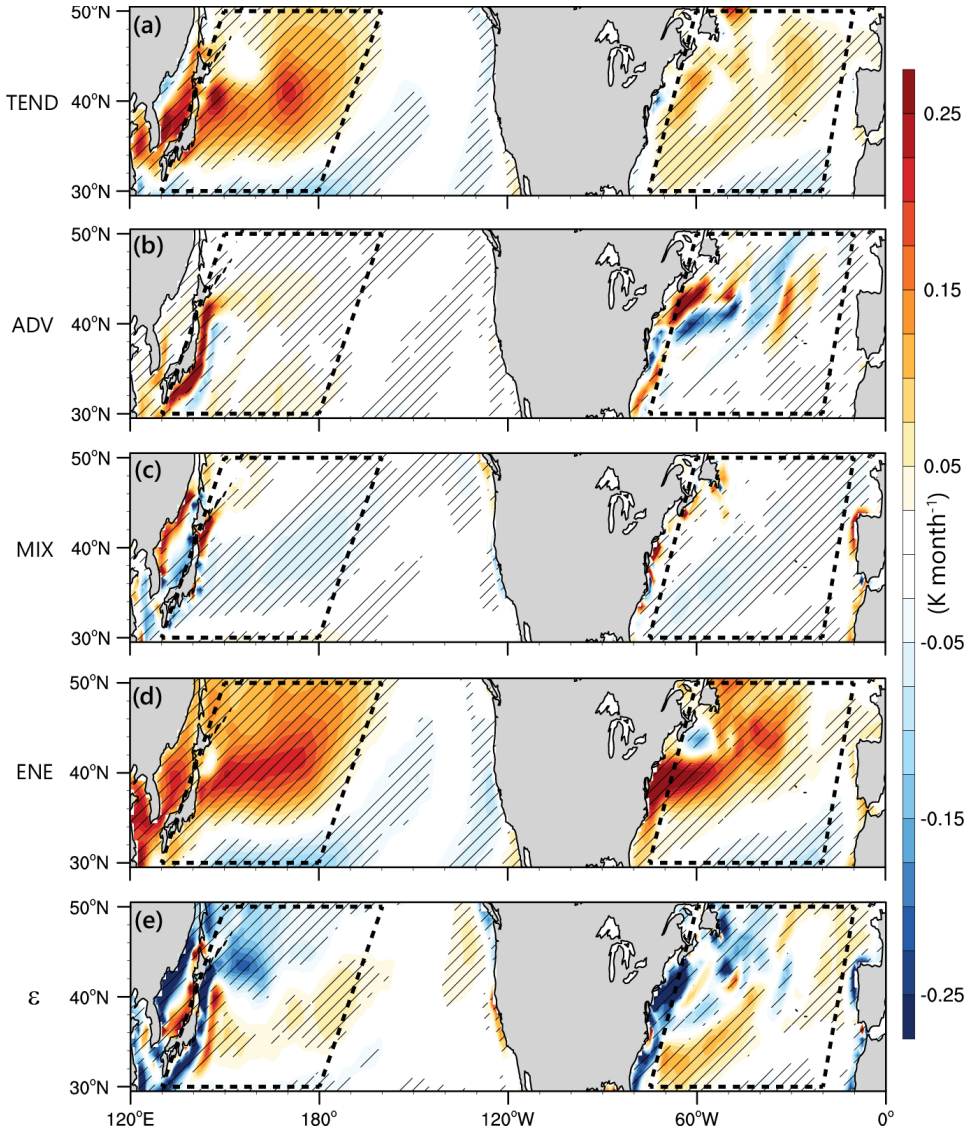

Fig. S10. Impact of TP heating on the energy budget of the ocean mixed layer over the North Pacific and Atlantic domains. Differences in JJA mean energy budget terms of the mixed layer as indicated in Eq. (1), as determined using cmip-hist minus cmip-TIP-sh0.5 experiments for 1850–2014. The stripe indicates significant differences at the 95% confidence level.

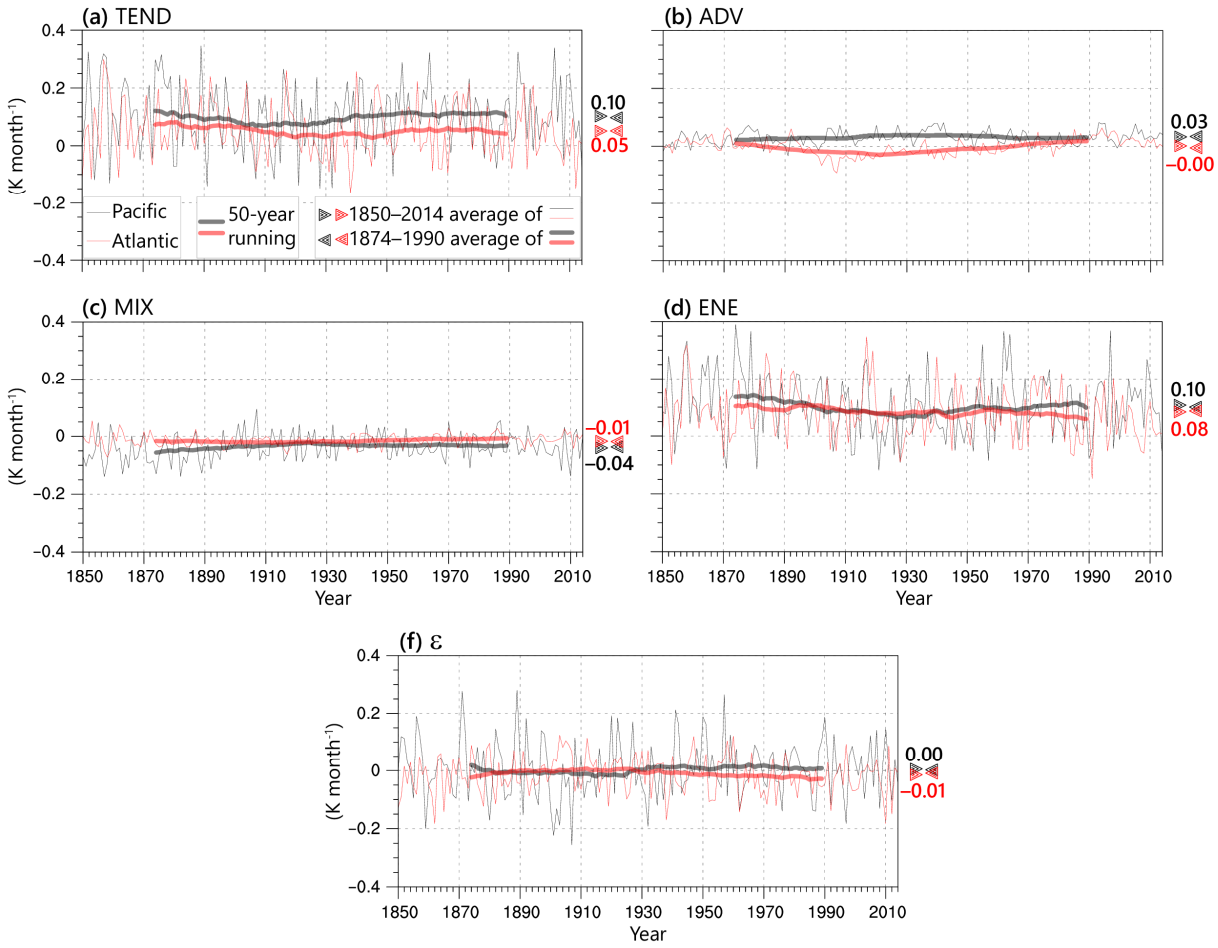

Fig. S11. Time-series of the differences in JJA mean energy budget terms (Eq. (1)) of mixed layer averaged over the Pacific (black) and Atlantic (red) domains shown in Fig. 3a, determined using cmip-hist minus cmip-TIP-sh0.5 experiments. The thin lines indicate the raw time-series for 1850–2014, while the thick lines indicate the 50-year-running-mean time-series for 1874–1990. The triangle markers indicate the temporal averages of the raw and 50-year-running-mean time-series, and the numbers indicate their average values. Fig. 4a also shows the averaged results for 1850–2014.

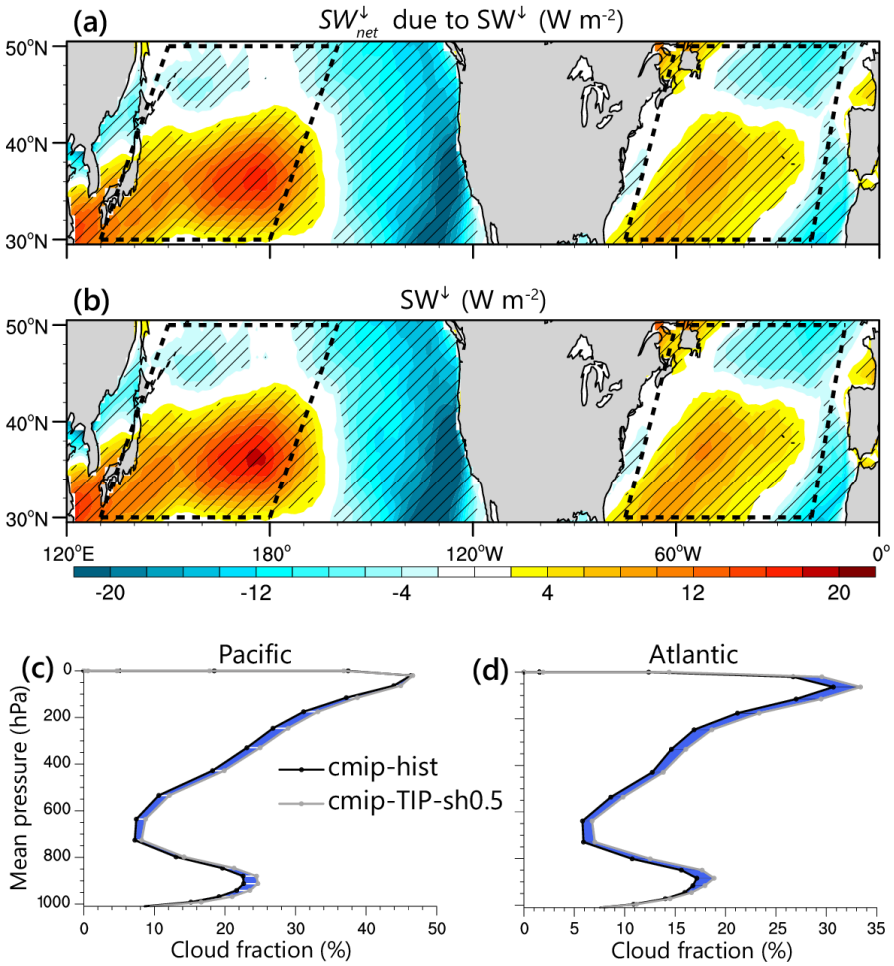

Fig. S12. Physical processes underlying the changes in net shortwave at the sea surface over the Pacific and Atlantic domains in summer. Differences in JJA mean (a) net shortwave ($SW^{\downarrow}_{net}$) due to downward shortwave ($SW^{\downarrow}$) formulated as the last right-hand term of $\delta(SW^{\downarrow}_{net}) \approx \underbrace{\delta(1-\alpha)\mathrm{S}W^{\downarrow}}_{\text{Albedo feedback}} + \underbrace{(1-\alpha)\delta(\mathrm{S}W^{\downarrow})}_{SW^{\downarrow}\text{ change}}$, (b) downward shortwave determined using cmip-hist minus cmip-TIP-sh0.5 experiments for 1850–2014. (c), (d) Regional mean cloud fraction averaged over the Pacific and Atlantic domains with positive value in (a) for cmip-hist and cmip-TIP-sh0.5 experiments, respectively. The blue shadings indicate that differences using the cmip-hist minus cmip-TIP-sh0.5 are negative, namely a reduced cloud fraction. The stripe indicates significant differences at the 95% confidence level.

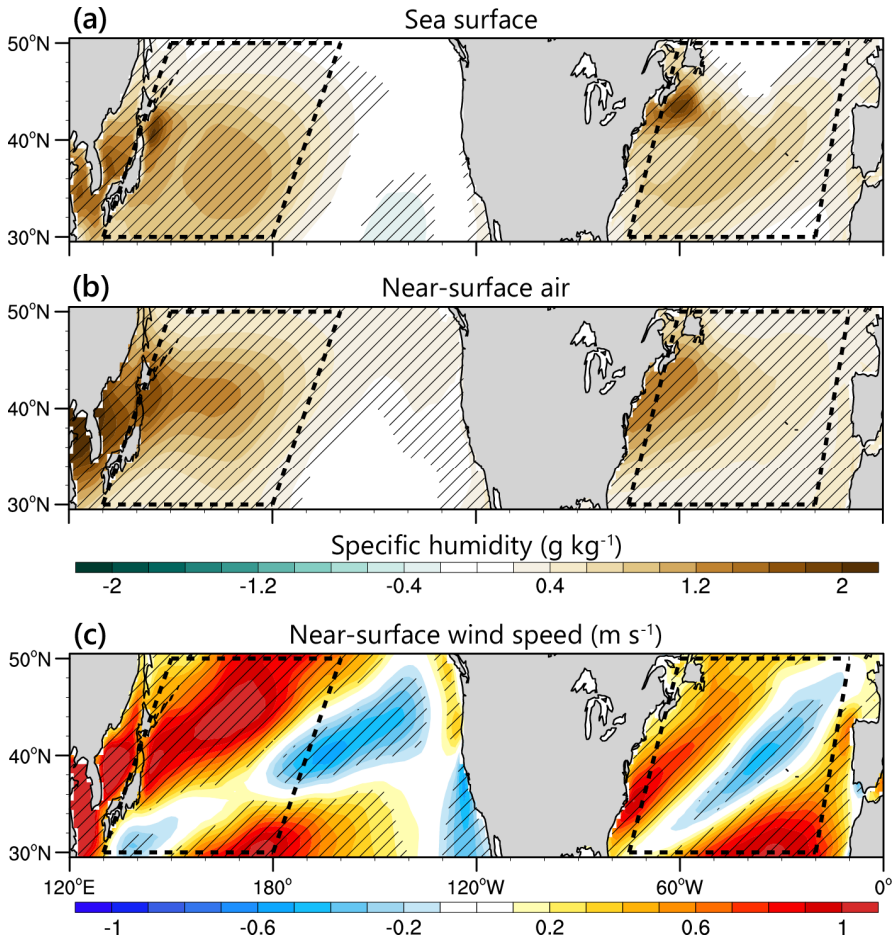

Fig. S13. Impact of TP heating on specific humidity and wind speed over the Pacific and Atlantic domains in summer. Differences in JJA mean (a) saturation specific humidity at sea surface temperature and (b) specific humidity of near-surface air determined using cmip-hist minus cmip-TIP-sh0.5 experiments for 1850–2014. The stripe indicates significant differences at the 95% confidence level. (c) Same as (b) but for near-surface wind speed.

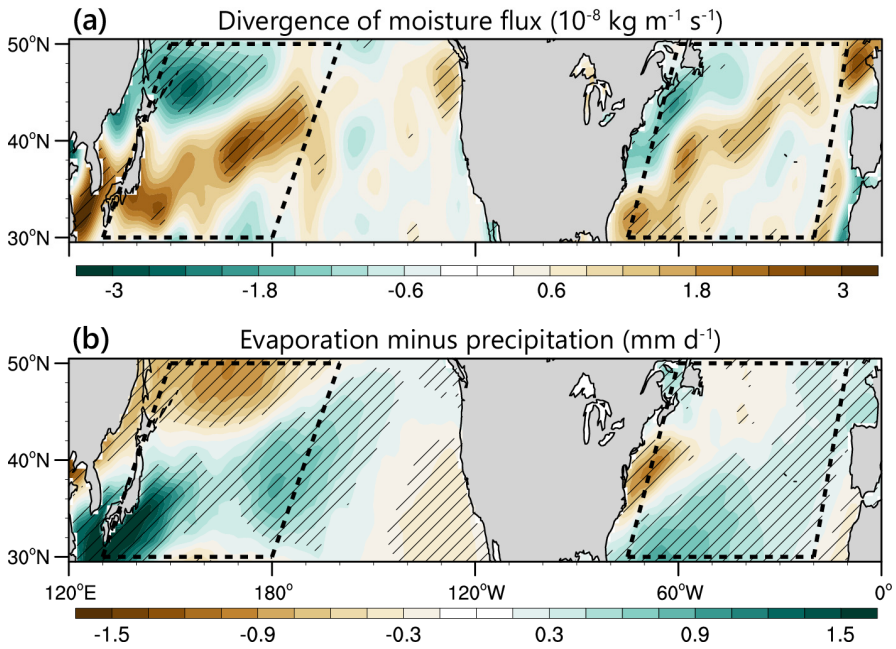

Fig. S14. Impact of TP heating on atmospheric specific humidity over the Pacific and Atlantic domains in summer. (a) Differences in JJA mean divergence of moisture flux, that is $\nabla_h \cdot \vec{M}$ ($\vec{M} = \rho \vec{V} q$; Section 2.3), at the near-surface, determined using cmip-hist minus cmip-TIP-sh0.5 experiments for 2000–2014. A negative value indicates convergence of atmospheric moisture. The stripe indicates significant differences at the 95% confidence level. (b) Same as (a) but for evaporation minus precipitation at the sea surface. A positive value indicates an increase in moisture source to the atmosphere from the sea surface. Since negative and positive values in (a) and (b) indicate positive contributions to atmospheric specific humidity, respectively, the color bars were opposite in (a) and (b).

Supplementary Table S1

Table S1. Information of models and experimental designs.

Models			
Name	Resolution		Institute
FGOALS-f3-L	Atmos: FAMIL2.2, c96 finite volume grid; 180 × 360 lat/lon; 32 vertical levels		IAP-LASG/China
FIO-ESM-2-0	Atmos: CAM4, 0.9 × 1.25 finite volume grid; 192 × 288 lat/lon; 26 vertical levels		FIO/China
CESM-2.1.3	Official tag: f09_f09_mg17 for amip and f09_g17 for cmip Atmos: CAM6, 0.9 × 1.25 finite volume grid; 192 × 288 lat/lon; 32 vertical levels Land: CLM5.0, 0.9 × 1.25 finite volume grid Ocean: POP2, finite volume grid 0.9 × 1.25_g × 1v7		NCAR/UCAR/USA
GMMIP experiments			
Name*	Designs	Time	Models
amip-hist	The historical run commences from January 1, 1861, with the external forcing defined by the observed values.	1861–2014	FGOALS-f3-L FIO-ESM-2-0
amip-TIP-nosh	Sensible heat is removed over the Asian topographies above 500 m [35]. The method used by FGOALS-f3-L is to set the vertical temperature diffusion term to zero in the atmospheric thermodynamic equation at the bottom boundary layer.	1970–2014	
CESM experiments			
amip-hist amip-TIP-nosh	Modified from the official case: FHIST amip-hist: same as GMMIP experiments except for integration time. amip-TIP-nosh: modified from amip-hist by removing the vertical diffusive sensible	1979–2014	

	heat on the entire column of the atmosphere, that is, all the model levels over the Asian topographies (same domain as in GMMIP).	(three-hourly outputs for 2000–2014)	CESM-2.1.3
amip-TIP-alb0.5	Same as amip-TIP-nosh, except for modification in surface albedo. The albedo is multiplied by 0.5; hence, TP heating increases relative to amip-hist.		
amip-TIP-sh0.5	Modified from amip-TIP-nosh by multiplying the sensible heat by 0.5, instead of setting a zero sensible heat.		
cmip-hist	Modified from the official case: BHIST Same as amip-hist but for a run with all components fully active and a different integration time.	1850–2014 (three-hourly outputs for 2000–2014)	
cmip-TIP-sh0.5	Modified from cmip-hist. The code modification is the same as in amip-TIP-sh0.5.		

* Experiment names follow the rules of the GMMIP.